

Optically Informed Searches of High-Energy Neutrinos from Interaction-Powered Supernovae

Tetyana Pitik,^{1,2}★ Irene Tamborra,¹† Massimiliano Lincetto,³ Anna Franckowiak³

¹Niels Bohr International Academy and DARK, Niels Bohr Institute, University of Copenhagen, Blegdamsvej 17, 2100 Copenhagen, Denmark

²Dipartimento di Fisica e Geologia, Università di Perugia, I.N.F.N. Sezione di Perugia, Via Pascoli, 06123 Perugia, Italy

³Ruhr University Bochum, Faculty of Physics and Astronomy, Astronomical Institute (AIRUB), Universitätsstraße 150, 44801 Bochum, Germany

6 July 2023

ABSTRACT

The interaction between the ejecta of supernovae (SNe) of Type II_n and a dense circumstellar medium (CSM) can efficiently generate thermal UV/optical radiation and lead to the emission of neutrinos in the 1–10³ TeV range. We investigate the connection between the neutrino signal detectable at the IceCube Neutrino Observatory and the electromagnetic signal observable by optical wide-field, high-cadence surveys to outline the best strategy for upcoming follow-up searches. We outline a semi-analytical model that connects the optical lightcurve properties to the SN parameters and find that a large peak luminosity ($L_{\text{peak}} \gtrsim 10^{43} - 10^{44} \text{ erg s}^{-1}$) and an average rise time ($t_{\text{rise}} \gtrsim 10 - 40$ days) are necessary for copious neutrino emission. Nevertheless, the most promising L_{peak} and t_{rise} can be obtained for SN configurations that are not optimal for neutrino emission. Such ambiguous correspondence between the optical lightcurve properties and the number of IceCube neutrino events implies that relying on optical observations only, a range of expected neutrino events should be considered (e.g. the expected number of neutrino events can vary up to two orders of magnitude for some among the brightest SNe II_n observed by the Zwicky Transient Facility up to now, SN 2020usa and SN 2020in). In addition, the peak in the high-energy neutrino curve should be expected a few t_{rise} after the peak in the optical lightcurve. Our findings highlight that it is crucial to infer the SN properties from multi-wavelength observations rather than focusing on the optical band only to enhance upcoming neutrino searches.

Key words: neutrinos – transients: supernovae – radiation mechanisms: non-thermal – acceleration of particles

1 Introduction

Astrophysical neutrinos with TeV–PeV energy are routinely observed by the IceCube Neutrino Observatory (Halzen & Kheirandish 2022; Ahlers & Halzen 2018; Abbasi et al. 2021a). While the sources of the observed neutrino flux are not yet known (Mészáros 2017; Vitagliano et al. 2020), a number of follow-up programs aims to link the observed neutrinos to their electromagnetic counterparts. In this context, the All-Sky Automated Survey for SuperNovae (ASAS-SN, Shappee et al. 2014; Kochanek et al. 2017) the Zwicky Transient Facility (ZTF, Bellm et al. 2019; Dekany et al. 2020) and the Panoramic Survey Telescope and Rapid Response System 1 (Pan-STARRS1, Chambers et al. 2016) perform dedicated target-of-opportunity searches for optical counterparts of neutrino events (Stein et al. 2023; Kankare et al. 2019; Necker et al. 2022), and vice versa the IceCube Neutrino Observatory looks for neutrinos in the direction of the sources discovered by optical surveys (see e.g. Abbasi et al. 2023; Abbasi et al. 2021b). The importance of such multi-messenger searches will be strengthened as large-scale transient facilities come online, such as the Rubin Observatory (Hambleton et al. 2022).

The putative coincidence of the high-energy neutrino event

IC200530A with the candidate superluminous supernova (SLSN) AT2019fdr (Pitik et al. 2022) ‡ makes searches of high-energy neutrinos from SNe timely. SLSNe are $\mathcal{O}(10\text{--}100)$ times brighter than standard core-collapse SNe (Gal-Yam 2019; Moriya et al. 2018), with kinetic energy sometimes larger than 10⁵¹ erg (Rest et al. 2011; Nicholl et al. 2020). SLSNe are broadly divided into two different spectral types: the ones with hydrogen emission lines (SLSNe II) and those without (SLSNe I), see e.g. (Gal-Yam 2012). The majority of SLSNe II displays strong and narrow hydrogen emission lines similar to those of the less luminous SNe II_n (Ofek et al. 2007; Rest et al. 2011; Smith et al. 2008) and often dubbed SLSNe II_n. Type II_n SNe are a sub-class of core-collapse SNe (Smith et al. 2011; Gal-Yam et al. 2007) characterized by bright and narrow Balmer lines of hydrogen in their spectra which persist for weeks to years after the explosion (Schlegel 1990; Filippenko 1997; Gal-Yam 2017). Type II_n SNe are expected to have a dense circumstellar material (CSM) surrounding the exploding star. The large luminosity of SNe II_n and the evidence of slowly moving material ahead of the ejecta indicate an efficient interaction of the ejecta with the CSM, which has long been considered a major energy source of the observed optical ra-

★ E-mail: tetyana.pitik@nbi.ku.dk

† E-mail: tamborra@nbi.ku.dk

‡ Note that the identification of the nature AT2019fdr is still under debate; it has been suggested that its properties might be compatible with the ones of a tidal disruption event (Reusch et al. 2022).

diation (Smith 2017; Blinnikov 2017). Given the similarities of the spectral characteristics, SLSNe IIn are deemed to be extreme cases of SNe IIn, albeit it is unclear whether SLSNe IIn are just the most luminous SNe IIn or they represent a separate population.

The collision between the expanding SN ejecta and the dense CSM gives rise to the forward shock, propagating in the dense SN environment, and the reverse shock moving backward in the SN ejecta. The plasma heated by the forward shock radiates its energy thermally in the UV/X-ray band. Depending on the column density of the CSM, energetic photons can be reprocessed through photo-electric absorption and/or Compton scattering downwards into the visible waveband, producing the observed optical lightcurve. Alongside the thermal population, a non-thermal distribution of protons and electrons can be created via diffusive shock acceleration.

Once accelerated, the relativistic protons undergo inelastic hadronic collisions with the non-relativistic protons of the shocked CSM, possibly leading to copious production of high-energy neutrinos and gamma-rays (Murase et al. 2011; Zirakashvili & Ptuskin 2016; Petropoulou et al. 2017; Sarmah et al. 2022). While gamma-rays are absorbed and reprocessed to a large extent in the dense medium (see, e.g., Sarmah et al. 2022), neutrinos stream freely and reach Earth without absorption (Murase et al. 2011; Katz et al. 2011; Zirakashvili & Ptuskin 2016; Cardillo et al. 2015; Kheirandish & Murase 2022; Sarmah et al. 2022, 2023; Brose et al. 2022). If detected, neutrinos with energies ≥ 100 TeV from an interacting SN would represent a smoking gun of acceleration of cosmic rays up to PeV energies (Bell 2013; Blasi 2013; Cristofari et al. 2020; Cristofari 2021).

In this paper, we consider SNe IIn and SLSNe IIn as belonging to the same population, distinguished primarily by the ejecta energetics and CSM density. We investigate how neutrino production depends on the characteristic quantities describing interaction-powered SNe and connect the main features of the optical lightcurve to the observable neutrino signal in order to optimize joint multi-messenger search strategies.

This work is organized as follows. Section 2 outlines the SN model. As for the CSM structure, we mostly focus on the scenario involving SN ejecta propagating in an extended envelope surrounding the progenitor with a wind-like density profile; we then extend our findings to the case involving SN ejecta propagating into a shell of CSM material with uniform density, which might result from a violent eruption shortly before the death of the star. In Sec. 3, we introduce the scaling relations for the SN lightcurve properties. Section 4 focuses on investigating the dependence of the maximum proton energy on the SN model parameters. In Sec. 5, after introducing the method adopted to compute the neutrino spectral energy distribution, the dependence of the total energy emitted in neutrinos is investigated as a function of the SN model parameters. Section 6 outlines the detection prospects of neutrinos by relying on two benchmark SLSNe IIn observed by ZTF and discusses the most promising strategies to detect neutrinos by relying on optical observations as well multi-messenger follow-up programs. Finally, our findings are summarized in Sec. 7. In addition, the dependence of the SN lightcurve properties and maximum proton energy on the SN model parameters are discussed in Appendix A and B, respectively. Moreover, details on the constant density scenario are provided in Appendix C.

2 Model for interaction-powered supernovae

In this section, we present the theoretical framework of our work. First, we describe the CSM configurations. Then, we focus on the

modeling of the interaction between the SN ejecta and the CSM, leading to the observed electromagnetic radiation. We also outline the SN model parameters and the related uncertainty ranges adopted in this work.

2.1 Modeling of the circumstellar medium

Observational data and existing theoretical models indicate that the matter envelope surrounding massive stars could be spherical in shape or exhibit bipolar shells, disks or clumps, with non-trivial density profiles. This is the result of steady or eruptive mass loss episodes, as well as binary interactions of the progenitor prior to the explosion (Smith 2017). To this purpose, we consider two CSM configurations: a uniform shell extended up to a radius $R_{\text{CSM},s}$ from the center of the explosion and a spherically symmetric shell with a wind radial profile extending smoothly from the progenitor surface up to an external radius ($R_{\text{CSM},w}$), as sketched in Fig. 1. Henceforth we name the former “shell scenario” (s) and the latter “wind scenario” (w).

We assume that the CSM has a mass M_{CSM} , radial extent R_{CSM} , and it is spherically distributed around the SN with a density profile described by a power-law function of the radius:

$$n_{\text{CSM}}(R) = \frac{\rho_{\text{CSM}}(R)}{m} = \frac{(3-s)M_{\text{CSM}}}{4\pi R_{\text{CSM}}^3} \left(\frac{R}{R_{\text{CSM}}} \right)^{-s} \equiv BR^{-s}, \quad (1)$$

where $m = \mu m_{\text{H}}$, with $\mu = 1.3$ (Lodders 2019) being the mean molecular weight for a neutral gas of solar abundance. We neglect the density dependence on the inner radius of the CSM and consider it to be the same as the progenitor radius $R_{\star} = 10^{13}$ cm $\ll R_{\text{CSM}}$. The case $s = 2$ represents the stellar wind scenario, whereas $s = 0$ denotes a shell of uniform density. We assume that the density external to the CSM shell ($R > R_{\text{CSM}}$) is much smaller than the one at $R < R_{\text{CSM}}$.

2.2 Shock dynamics

After the SN explodes, and the shock wave passes through the stellar layers, the ejecta gas evolves to free homologous expansion. Relying on numerical simulations (e.g., Matzner & McKee 1999), we assume that during this phase the outer part of the SN ejecta has a power-law density profile (Chevalier & Fransson 1994; Moriya et al. 2013):

$$\rho_{\text{ej}}(R, t) = g_n t^{n-3} R^{-n}, \quad (2)$$

with

$$g_n = \frac{1}{4\pi(n-\delta)} \frac{[2(5-\delta)(n-5)E_k]^{(n-3)/2}}{[(3-\delta)(n-3)M_{\text{ej}}]^{(n-5)/2}}, \quad (3)$$

where E_k is the total SN kinetic energy, M_{ej} is the total mass of the SN ejecta, n is the density slope of the outer part of the ejecta, and δ the slope of the inner one. The parameter n depends on the progenitor properties and the nature (convective or radiative) of the envelope; $n \approx 12$ is typical of red supergiant stars (Matzner & McKee 1999), while lower values are expected for more compact progenitors. In this work, we adopt $n = 10$ and $\delta = 1$, following Suzuki et al. (2020).

The interaction between the SN ejecta and the CSM results in a forward shock moving in the CSM and a reverse shock propagating back in the stellar envelope. For our purposes, only the forward shock is relevant. It is indeed estimated that the contribution of the reverse shock to the electromagnetic emission, as well as its efficiency in accelerating particles during the timescales of interest, is significantly lower than the one of the forward shock (Ellison et al. 2007; Patnaude

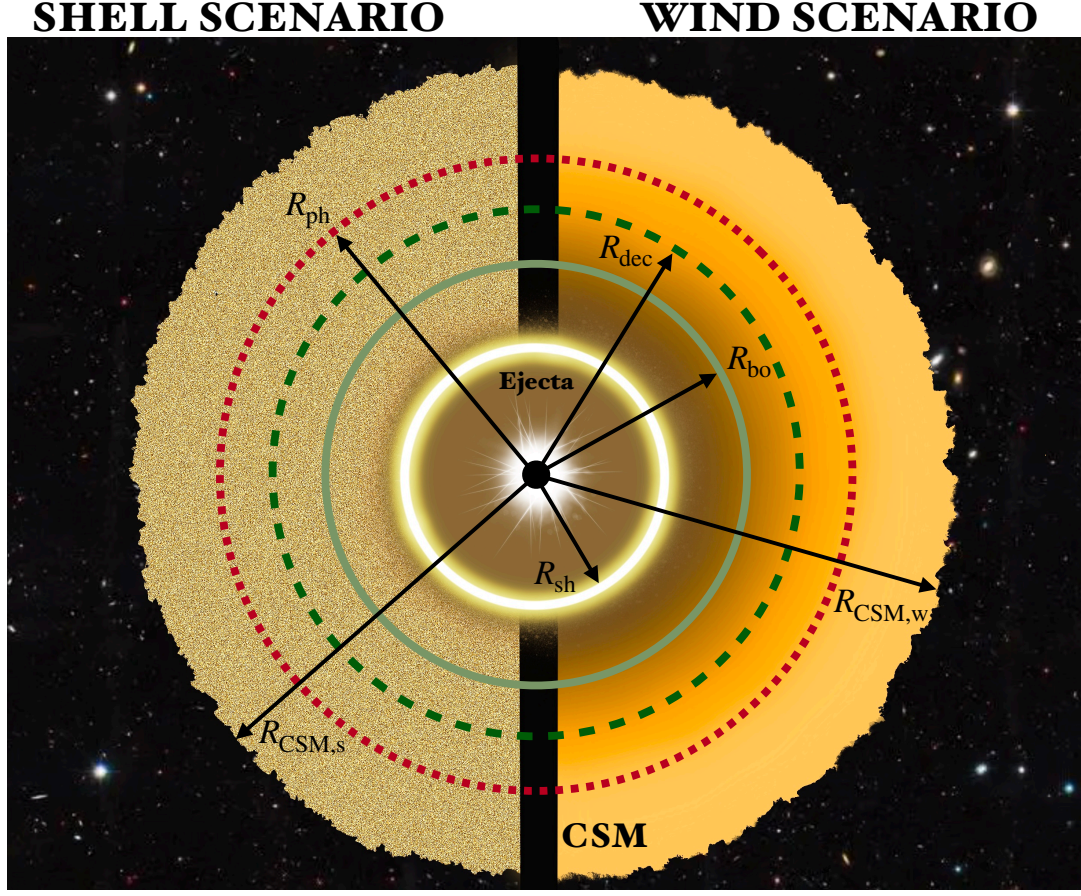


Figure 1. Schematic representation of an interaction-powered SN, under the assumption of spherical symmetry. The central compact object (in black) is surrounded by the SN ejecta (brown) and a compact shell extended up to $R_{\text{CSM},s}$ ($R_{\text{CSM},w}$) from the center of explosion for the shell scenario on the left (and the wind scenario, on the right). For the wind density profile, the color gradient tracks the density gradient (from darker to lighter hues as the density decreases). The region of interaction marked through the yellow-white circle represents the forward shock R_{sh} that propagates radially outwards. The solid olive line marks the position of the breakout radius (R_{bo}), where the first light leaks out, and the shock becomes collisionless. The dashed dark green line marks the location of the deceleration radius of the ejecta (R_{dec}). The latter is located at radii smaller than R_{CSM} (as in this sketch) for a relatively large CSM mass compared to the ejecta mass or radii larger than R_{CSM} for massive ejecta and rarefied CSM; note that we could have $R_{\text{dec}} < R_{\text{bo}}$ for extremely large $M_{\text{CSM}}/M_{\text{ej}}$. The dashed bordeaux line represents the photospheric radius R_{ph} , where the radiation decouples from the CSM matter and stream in the outer space freely.

& Fesen 2009; Schure et al. 2010; Slane et al. 2015; Sato et al. 2018; Suzuki et al. 2020; Zirakashvili & Ptuskin 2016).

Following Chevalier (1982); Moriya et al. (2013), we assume that the thickness of the shocked region is much smaller than its radius, R_{sh} . As long as the mass of the SN ejecta is larger than the swept-up CSM mass, which we define as the ejecta dominated phase (or free expansion phase), the expansion of the forward shock radius is described by (Moriya et al. 2013):

$$R_{\text{sh}}(t) = R_{\star} + \left[\frac{(3-s)(4-s)}{(n-4)(n-3)} \frac{g_n}{B} \right]^{\frac{1}{n-s}} t^{\frac{n-3}{n-s}}, \quad (4)$$

with B defined as in Eq. 1, and hereafter we assume that the interaction starts at $t = 0$.

When the swept-up CSM mass becomes comparable to the SN ejecta mass, the ejecta start to slow down, entering the CSM dominated phase. This happens at the deceleration radius, defined as the radius R_{dec} at which $\int_{R_{\star}}^{R_{\text{dec}}} 4\pi R^2 \rho_{\text{CSM}} dR = M_{\text{ej}}$, namely

$$R_{\text{dec}} = \left[\frac{3-s}{4\pi B} M_{\text{ej}} + R_{\star}^{3-s} \right]^{\frac{1}{3-s}}. \quad (5)$$

According to the relative ratio between M_{ej} and M_{CSM} , the deceleration

can occur inside or outside the CSM shell (where a dilute stellar wind surrounds the collapsing star). After this transition, the forward shock evolves as (Suzuki et al. 2020):

$$R_{\text{sh}}(t) = R_{\text{dec}} \left(\frac{t}{t_{\text{dec}}} \right)^{\frac{2}{5-s}}. \quad (6)$$

Differentiating Eqs. 4 and 6, we obtain the forward shock velocity as a function of time:

$$v_{\text{sh}}(t) = \frac{dR_{\text{sh}}(t)}{dt} = \begin{cases} \frac{n-3}{n-s} \left[\frac{(3-s)(4-s)}{(n-4)(n-3)} \frac{g_n}{B} \right]^{\frac{1}{n-s}} t^{\frac{s-3}{n-s}} & R < R_{\text{dec}} \\ \frac{2}{5-s} R_{\text{dec}} \left(\frac{t}{t_{\text{dec}}} \right)^{\frac{s-3}{5-s}} & R \geq R_{\text{dec}} \end{cases}. \quad (7)$$

We consider the dynamical evolution under the assumption that the shock is adiabatic for two reasons. First, we want to compare our results with the literature on the properties of the SN lightcurves extrapolated by relying on semi-analytic models for the adiabatic expansion, see e.g. Suzuki et al. (2020). Second, it has been shown that, in the radiative regime, R_{sh} has the same temporal dependence as the self-similar solution $\propto t^{(n-3)/(n-s)}$ in the free expansion

phase with radiative losses having a strong impact on the evolution of the shock (Moriya et al. 2013).

While the shock propagates in the CSM, the ejecta kinetic energy is dissipated in the interaction and converted into thermal energy. The shock-heated gas behind the forward shock front cools by emitting thermal energy in the form of free-free radiation (thermal bremsstrahlung). However, if the CSM ahead of the shock is optically thick, such radiation is trapped and remains confined until the shock breakout, which occurs at the breakout radius (R_{bo}). The latter is computed by solving the following equation for the Thomson optical depth (due to photon scattering on electrons) §:

$$\tau_T = \int_{R_{\text{bo}}}^{R_{\text{CSM}}} \rho_{\text{CSM}}(R) \kappa_{\text{es}} dR = \frac{c}{v_{\text{sh}}}, \quad (8)$$

where κ_{es} is the electron scattering opacity, c the speed of light, and v_{sh} is defined in Eq. 7. If $R_{\text{bo}} \leq R_{\star}$, $R_{\text{bo}} = R_{\star}$.

We make use of the assumption of constant opacity, valid for electron Compton scattering. The value of κ_{es} , which depends on the composition, typically ranges from $\kappa_{\text{es}} \sim 0.2 \text{ cm}^2 \text{ g}^{-1}$ for hydrogen-free matter to $\kappa_{\text{es}} \sim 0.4 \text{ cm}^2 \text{ g}^{-1}$ for pure hydrogen. We consider solar composition of the CSM, namely $\kappa_{\text{es}} = 0.2(1 + X_{\text{H}}) \simeq 0.34 \text{ cm}^2 \text{ g}^{-1}$ (Rybicki & Lightman 1986), where $X_{\text{H}} = 0.73$ is the hydrogen mass fraction (Lodders 2019).

As long as $\tau_T \gg c/v_{\text{sh}}$, the shock is radiation-mediated (energy density of the radiation is larger than the energy density of the gas) and radiation pressure rather than plasma instabilities mediate the shock. In this regime, non-thermal particle acceleration is inefficient, since a shock width much larger than the particle gyro-radius hinders standard Fermi acceleration (Weaver 1976; Levinson & Bromberg 2008; Katz et al. 2011; Murase et al. 2011). Furthermore, diffusion can be neglected. When $\tau_T < c/v_{\text{sh}}$, the shock becomes collisionless, and efficient particle acceleration begins.

2.3 Interaction-powered supernova emission

When the forward shock propagates in the region with $\tau_T < c/v_{\text{sh}}$, the gas immediately behind the shock is heated to a temperature T_{sh} . Assuming electron-ion equilibrium, such a temperature can be obtained by the Rankine–Hugoniot conditions:

$$k_B T_{\text{sh}} = 2 \frac{(\gamma - 1)}{(\gamma + 1)^2} \tilde{\mu} m_{\text{H}} v_{\text{sh}}^2 \approx 118 \text{ keV} \left(\frac{v_{\text{sh}}}{10^9 \text{ cm s}^{-1}} \right)^2, \quad (9)$$

where $\gamma = 5/3$ is the adiabatic index of the gas. We adopt mean molecular weight $\tilde{\mu} = 0.6$; such a choice is appropriate for fully ionized CSM with solar composition as it is the case for the matter right behind the shock (this is different from Eq. 1 where the CSM is assumed to be neutral). The thermal emission properties of the shock-heated material can be fully characterized by the shock velocity v_{sh} and the other parameters characterizing the CSM (Margalit et al. 2022).

The observational signatures of the SN lightcurve and spectra depend on the radiative processes, which shape the thermal emission. The main photon production mechanism is free-free emission of the shocked electrons, whose typical timescale is (Draine 2011):

$$t_{\text{cool}} = \frac{3k_B T_{\text{sh}}}{2n_{\text{sh}} \Lambda(T)}, \quad (10)$$

§ Note that we do not adopt the common approximation $R_{\text{bo}} \equiv (\kappa_{\text{es}} K v_{\text{sh}})/c$, valid only when $R_{\text{bo}} \ll R_{\text{CSM}}$ and v_{sh} independent on R (Chevalier & Irwin 2011).

where k_B is the Boltzmann constant, $n_{\text{sh}} = 4n_{\text{CSM}}$ is the density of the shocked region. The factor 4 comes from the Rankine–Hugoniot jump conditions across a strong non-relativistic shock. $\Lambda(T)$ is the cooling function (in units of $\text{erg cm}^3 \text{ s}^{-1}$) that captures the physics of radiative cooling (Chevalier & Fransson 1994):

$$\Lambda(T) = \begin{cases} 6.2 \times 10^{-19} T^{-0.6} & 10^5 < T \lesssim T_{\star} \\ 2.5 \times 10^{-27} T^{0.5} & T > T_{\star} \end{cases} \quad (11)$$

The temperature $T_{\star} = 4.7 \times 10^7 \text{ K}$ represents the transition from the regime where free-free emission is dominant ($T \gtrsim T_{\star}$) to the one where line-emission becomes relevant ($T \lesssim T_{\star}$). If the free-free cooling timescale is shorter than the dynamical time, the shock becomes radiative. In this regime, particles behind the shock cool within a layer of width $(t_{\text{cool}}/t_{\text{dyn}})R_{\text{sh}}$.

Although the radiation created during the interaction could diffuse from the CSM, the presence of dense pre-shock material causes the emitted photons to experience multiple scattering episodes before they reach the photosphere (defined as the surface where $\tau_T = 1$):

$$R_{\text{ph}} = \left[\frac{s-1}{\kappa_{\text{es}} B} + R_{\text{CSM}}^{1-s} \right]^{\frac{1}{1-s}}. \quad (12)$$

The dominant mechanisms responsible for the photon field degradation in the medium are photoelectric absorption and Compton scattering, that generate inelastic energy transfer from photons to electrons during propagation. The result of such energy losses is that the bulk of thermal X-ray photons (see Eq. 9) is absorbed and reprocessed via continuum and line emission in the optical. This phenomenon is strongly dependent on the CSM mass and extent, as well as on the stage of the shock evolution.

Alongside bremsstrahlung photons, a collisionless shock may produce non-thermal radiation from a relativistic population of electrons accelerated through diffusive shock acceleration. Synchrotron emission of these electrons is mainly expected in the radio band; it has been shown that the CSM mass and radius play an important role in defining the radio peak time and luminosity (see, e.g., Petropoulou et al. 2016).

2.4 Supernova model parameters

The parameters characterizing SNe/SLSNe of Type IIn carry large uncertainties. For our benchmark SN model, we take into account uncertainty ranges for the SN energetics, CSM and ejecta masses, as well as the CSM radial extent as summarized in Table 1. A number of other uncertainties can significantly impact the observational features, e.g. the composition and geometry of the stellar environment or the stellar structure.

The electromagnetic emission of SLSNe IIn can be explained invoking a massive CSM shell with enough inertia to decelerate and dissipate most of the kinetic energy of the ejecta: $M_{\text{CSM}} \gtrsim 40 M_{\odot}$, $M_{\text{ej}} \gtrsim 50 M_{\odot}$, and $E_{\text{k}} \gtrsim 10^{52} \text{ erg}$ have been invoked for SLSNe in the tail of the distribution (see e.g. Nicholl et al. 2020; Drake et al. 2011), consistent with pair-instability SN models. On the other hand, SNe IIn may result from the interaction with a less dense surrounding medium, or simply fall in the class of less powerful explosions, with $M_{\text{CSM}} \lesssim 5 M_{\odot}$, $E_{\text{k}} \sim \text{a few } 10^{51} \text{ erg}$, and $M_{\text{ej}} \lesssim 50 M_{\odot}$ (see, e.g. Chatzopoulos et al. 2013).

To encompass the wide range of SN properties and the related uncertainties, we consider the space of parameters summarized in Table 1. In the following, we systematically investigate the dependence of the lightcurve features, such as the rise time and the peak luminosity on the SN parameters. For the sake of completeness, we

Table 1. Supernova model parameters for the SN wind and shell scenarios. The reference values adopted for our benchmark SN model are provided together with the uncertainty range for the most uncertain parameters.

Parameter	Symbol	Benchmark value	Parameter range
Accelerated proton energy fraction	ε_p	0.1	—
Magnetic energy density fraction	ε_B	3×10^{-4}	—
Proton spectral index	k	2	—
External ejecta density slope	n	10	—
Internal ejecta density slope	δ	1	—
Kinetic energy	E_k	10^{51} erg	10^{50} – 10^{53} erg
Ejecta mass	M_{ej}	$10 M_\odot$	1– $70 M_\odot$
CSM mass	M_{CSM}	$10 M_\odot$	1– $70 M_\odot$
CSM radius	R_{CSM}	10^{16} cm	5×10^{15} – 10^{17} cm

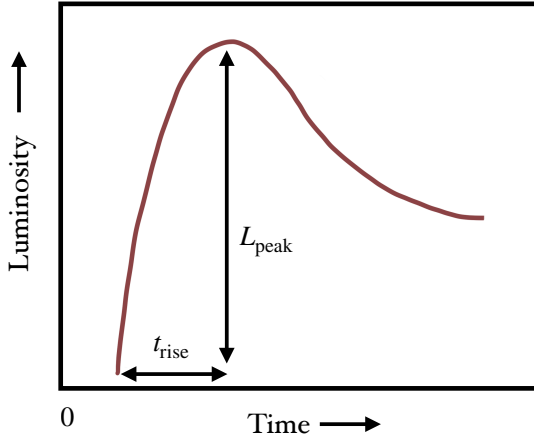


Figure 2. Sketch of the SN luminosity evolution (in arbitrary units) resulting from the interaction of the SN shock with the dense CSM. The origin ($t = 0$) coincides with the SN explosion time. Note that t_{rise} is defined from the time of the shock breakout.

choose generous uncertainty ranges, albeit most of the observed SN events do not require kinetic energies larger than 10^{52} erg or CSM masses larger than $50 M_\odot$ for example.

3 Scaling relations for the photometric supernova properties

In this section, we introduce the scaling relations for the peak luminosity and the rise time of a SN lightcurve powered by shock interaction. Such relations connect these two observable quantities to the SN model parameters.

We are interested in the shock evolution after shock breakout, when $\tau_T < c/v_{\text{sh}}$. During this regime, the lightcurve is powered by continuous conversion of the ejecta kinetic energy—see e.g. Chatzopoulos et al. (2012); Ginzburg & Balberg (2012); Moriya et al. (2013). Such a phase, however, reproduces the decreasing-flat part of the SN lightcurve at later times (see Fig. 2), while the initial rising part of the optical signal can be explained considering photon diffusion in the optically thick region—see e.g. Chevalier & Irwin (2011); Chatzopoulos et al. (2012).

Since we are interested in exploring a broad space of SN model parameters, we rely on semi-analytical expressions for the characteristic quantities that describe the optical lightcurve, namely the bolometric luminosity peak L_{peak} and the rise time to the peak t_{rise} (see Fig. 2). By performing 1D radiation-hydrodynamic simulations for a large region of the space of parameters, Suzuki et al. (2020) fitted the

output of their numerical simulations with semi-analytical scaling relations, investigating the relation between L_{peak} and t_{rise} . In this way, it is possible to analyze the dependence of the lightcurve properties on the parameters characterizing the SN interaction, i.e. the kinetic energy of the ejecta (E_k), the mass of the ejecta (M_{ej}), the mass of the CSM (M_{CSM}), and the extent of the CSM (R_{CSM}). Suzuki et al. (2020) found that the semi-analytical scaling relations describe relatively well the numerical results, once accounting for some calibration factors. In this section, we review the scaling relations we adopt throughout our work.

As the forward shock propagates in the CSM, the post-shock thermal energy per unit radius coming from the dissipation of the kinetic energy is given by

$$\mathcal{E}_k(R) = \frac{dE_k}{dR} = \frac{9}{8} \pi R^2 v_{\text{sh}}^2(R) \rho_{\text{CSM}}(R). \quad (13)$$

where we have used the Rankine–Hugoniot jump conditions across a strong non-relativistic shock that provide a compression ratio $\simeq 4$.

We define the bolometric peak luminosity as the kinetic power of the shock at breakout:

$$L_{\text{peak}} = \left. \frac{dE_k}{dt} \right|_{R_{\text{bo}}} = \frac{9}{8} \pi R_{\text{bo}}^2 v_{\text{sh}}^3(R_{\text{bo}}) \rho_{\text{CSM}}(R_{\text{bo}}). \quad (14)$$

When the shock is still crossing the CSM envelope, the radiated photons undergo multiple scatterings before reaching the photosphere. The diffusion coefficient is $D(R) \sim c\lambda(R)$, with $\lambda(R) = 1/\kappa_{\text{es}}\rho_{\text{CSM}}(R)$ being the photon mean free path. The time required to diffuse from R_{bo} to the photosphere R_{ph} represents the rise time of the bolometric lightcurve (Ginzburg & Balberg 2012) ¶:

$$t_{\text{rise}} \approx \int_{R_{\text{bo}}}^{R_{\text{ph}}} \frac{d(R - R_{\text{bo}})^2}{D(R)} \sim \int_{R_{\text{bo}}}^{R_{\text{ph}}} \frac{2(R - R_{\text{bo}})\kappa_{\text{es}}\rho_{\text{CSM}}(R)dR}{c}. \quad (15)$$

Furthermore, after the forward shock breaks out from the optically thick part of the CSM at R_{ph} , its luminosity is expected to be primarily emitted in the UV/X-ray region of the spectrum, and not in the optical (Ginzburg & Balberg 2012). Hence, we consider the photospheric radius as the radius beyond which the optical emission is negligible. Distinguishing the free-expansion regime (FE, $M_{ej} \gg M_{\text{CSM}}$) and the blast-wave regime (BW, $M_{ej} \ll M_{\text{CSM}}$) (Suzuki et al. 2020) ¶, the

¶ This definition of the rise time is valid as long as the CSM is dense enough to cause shock breakout in the CSM wind. If this is not the case, the breakout occurs at the surface of the collapsing star; the CSM masses responsible for this scenario are not considered in our investigation.

¶ Note that this distinction should not be confused with the ejecta/CSM-dominated phases introduced in Sec. 2.2.

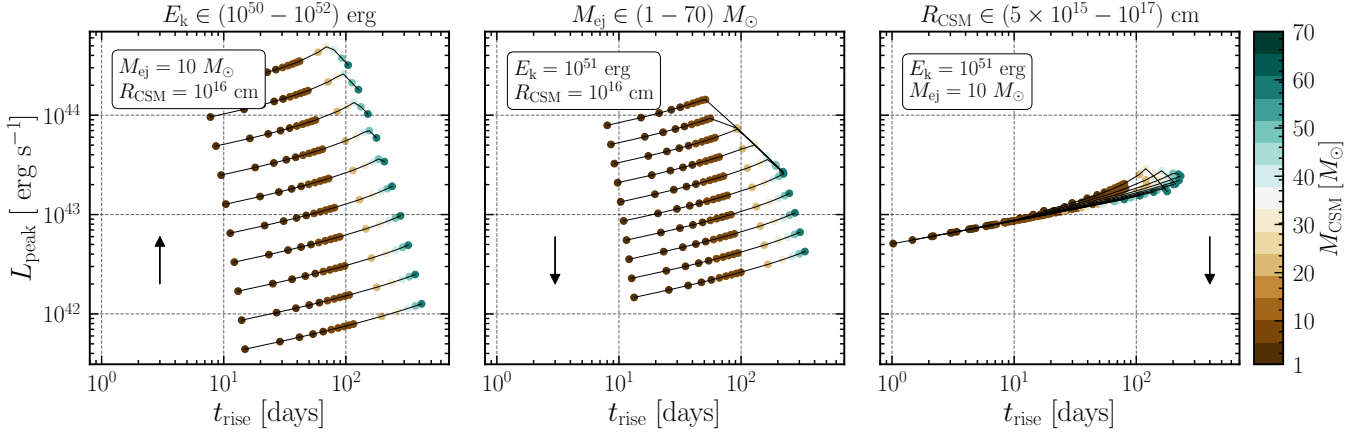


Figure 3. Bolometric peak luminosity as a function of the rise time, for fixed M_{ej} and R_{CSM} (left panel, and varying E_k), fixed E_k and R_{CSM} (middle panel, and varying M_{ej}), and fixed E_k and M_{ej} (right panel, and varying R_{CSM}). In each panel, the arrow points in the direction of increasing values of the parameter indicated on top of the plot (e.g. in the left panel, the highest curve is obtained with the the largest kinetic energy, 10^{52} erg). For each curve, the color hues mark the variation of M_{CSM} . The longest rise times and brightest lightcurves are obtained for large kinetic energies (left panel), the low ejecta mass (middle panel), large CSM mass and small CSM extension (right panel). Models with intermediate t_{rise} can reach the largest peak luminosities. The largest dispersion of long-lasting interaction-powered SNe can be achieved by increasing the kinetic energy. By keeping E_k fixed, an upper limit on L_{peak} is expected for different M_{ej} and R_{CSM} .

kinetic energy dissipated during the shock evolution in the optically thick region is:

$$E_{\text{diss,thick}} = \begin{cases} \int_{R_\star}^{R_{\text{ph}}} \mathcal{E}_k(R) dR & \text{for FE} \\ \frac{(3-s)(\gamma+1)}{3+9\gamma-2s-2\gamma s} E_k & \text{for BW.} \end{cases} \quad (16)$$

Part of this energy is converted into thermal energy and radiated. The fraction radiated in the band of interest depends on multiple factors, including the cooling regime of the shock during the evolution, as well as the ionization state and CSM properties. We parametrize these unknowns by introducing the fraction ε_{rad} of the total dissipated energy $E_{\text{diss,thick}}$ that is emitted in the optical band. We note that we adopt a definition of the rise time which differs from the Arnett’s rule employed in Suzuki et al. (2020), leading to comparable results, except for extremely low values of R_{CSM} ($\sim 10^{15}$ cm), which we do not consider in this work. In Appendix A we provide illustrative examples of the dependence of L_{peak} , t_{rise} , and $E_{\text{diss,thick}}$ on the parameters characterizing the SN lightcurve for the wind CSM configuration ($s = 2$).

Figure 3 shows L_{peak} as a function of t_{rise} , obtained by adopting the semi-analytic modeling in the FE and BW regimes. We note that the largest dispersion in the peak luminosity for long-lasting SNe/SLSNe II is obtained by varying the ejecta kinetic energy (left panel). For fixed kinetic energy, we see that the SN models corresponding to different ejecta mass (middle panel) all converge to approximately similar peak luminosity for longer t_{rise} , which corresponds to the region where the shock evolution is in the BW regime. This means that there is an upper limit on L_{peak} for a certain t_{rise} , and the only way to overcome this limit is by increasing the ejecta energy. Changes in R_{CSM} (right panel) lead to the smallest dispersion in L_{peak} among all the considered parameters. It is the variation of the kinetic energy that causes the largest spread in L_{peak} . Our findings are in agreement with the ones of Suzuki et al. (2020).

4 Maximum proton energy

In order to estimate the number of neutrinos and their typical energy during the shock evolution in the CSM, we first need to examine the energy gain and loss mechanisms that determine the maximum energy up to which protons can be accelerated. We assume first-order Fermi acceleration, which takes place at the shock front with the accelerating particles gaining energy as they cross the shock front back and forth.

In the Bohm limit, where the proton mean free path is equal to its gyroradius $r_g = \gamma_p m_p c^2 / eB$, the proton acceleration timescale is $t_{\text{acc}} \sim 6\gamma_p m_p c^3 / eB v_{\text{sh}}^2$ (Protheroe & Clay 2004; Tammi & Duffy 2009; Caprioli & Spitkovsky 2014, see, e.g.), where $B = \sqrt{9\pi \varepsilon_B v_{\text{sh}}^2 \rho_{\text{CSM}}}$ is the turbulent magnetic field in the post-shock region, whose energy density is assumed to be a fraction ε_B of the post-shock thermal energy $U_{\text{th}} = (9/8)v_{\text{sh}}^2 \rho_{\text{CSM}}$.

The maximum energy up to which protons can be accelerated is determined by the competition between particle acceleration and energy loss mechanisms, such that $t_{\text{acc}} \leq t_{\text{p,cool}}$, with $t_{\text{p,cool}}$ being the total proton cooling time. The relevant cooling times are the advection time ($t_{\text{adv}} \sim \Delta R_{\text{acc}} / v_{\text{sh}}$, with ΔR_{acc} being the width of the acceleration region) and the proton-proton interaction time ($t_{\text{pp}} = (4k_{\text{pp}}\sigma_{\text{pp}}n_{\text{CSM}}c)^{-1}$, where we assume constant inelasticity $k_{\text{pp}} = 0.5$ and energy-dependent cross-section $\sigma_{\text{pp}}(E_p)$ (Zyla et al. 2020)).

As pointed out in Fang et al. (2020), taking $\Delta R_{\text{acc}} \sim R_{\text{sh}}$ may be appropriate for adiabatic shocks only. If the shock is radiative, particles in the post-shock region cool via free-free emission within a layer of width $\sim (t_{\text{cool}}/t_{\text{dyn}})R_{\text{sh}}$ (see Sec. 2.3), making the gas far from the shock quasi-neutral, and thus hindering the magnetic field amplification crucial in the acceleration mechanism (Bell 2004). Hence, we adopt $\Delta R_{\text{acc}} = (t_{\text{cool}}/t_{\text{dyn}})R_{\text{sh}}$ for $t_{\text{cool}} < t_{\text{dyn}}$, and $\Delta R_{\text{acc}} = R_{\text{sh}}$ otherwise.

The total proton cooling time can thus be written as $t_{\text{p,cool}}^{-1} = t_{\text{pp}}^{-1} + \max[t_{\text{dyn}}^{-1}, t_{\text{cool}}^{-1}]$. It is important to note that relativistic protons in the shocked region may also interact with the ambient photons via $p\gamma$ interactions. However, we ignore such an energy loss

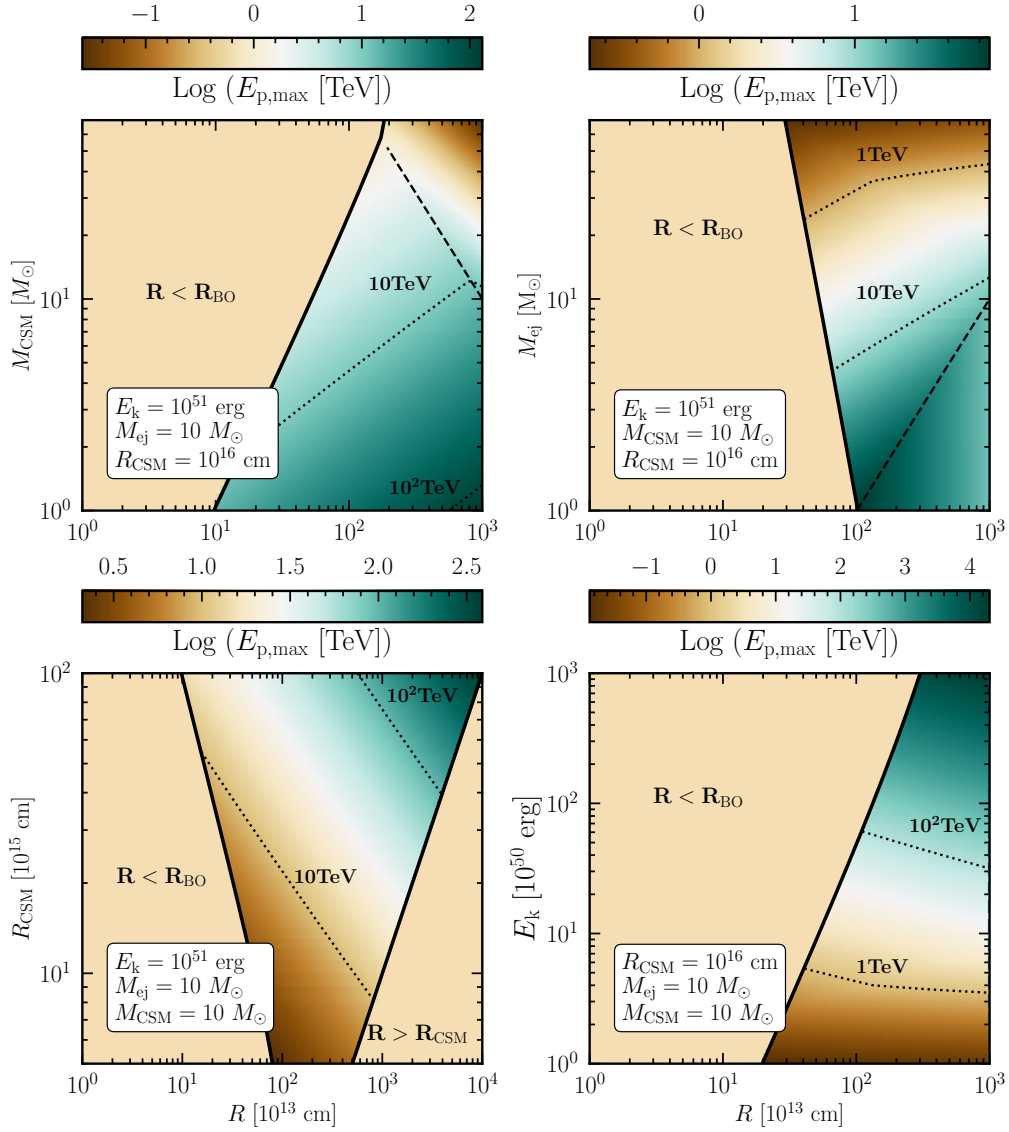


Figure 4. Contour plots of the maximum proton energy for the wind scenario in the plane spanned by the distance from the central engine and M_{CSM} (top left panel), M_{ej} (top right panel), R_{CSM} (bottom left panel), and E_k (bottom right panel), while the remaining three SN model parameters are fixed to their benchmark values. In each panel, the dashed line marks the deceleration radius, after which $E_{p,\text{max}}$ decreases. The maximum proton energy increases with the radius (and therefore with time). Indeed, the largest $E_{p,\text{max}}$ is obtained in the late stages of the shock evolution. Large R_{CSM} and M_{ej} , and small M_{CSM} and E_k lead to the longest interaction times. This statement is not true when $M_{\text{ej}} \ll M_{\text{CSM}}$ (see left upper and bottom right panels). The black solid lines define the edges of the interaction region, $R_{\text{bo}} \leq R \leq R_{\text{CSM}}$.

channel, by relying on the findings of [Murase et al. \(2011\)](#); [Fang et al. \(2020\)](#) that showed that $p\gamma$ interactions can be neglected for a wide range of SN parameters.

Figure 4 shows contours of $E_{p,\text{max}}$ for the wind scenario. The black solid lines mark the edges of the interaction region, hence Fig. 4 also provides an idea of the typical interaction duration. Fixing three of the SN model parameters to their benchmark values (see Table 1), the shortest period of interaction is obtained for small R_{CSM} and large M_{CSM} , or small M_{ej} and large E_k . In fact in both cases the shock breakout is delayed. The maximum proton energy increases with the radius, and the largest $E_{p,\text{max}}$ can be obtained in the late stages of the shock evolution, hinting that high-energy neutrino production should be favored at later times after the bolometric peak.

The breaks observed in the contour lines in the upper and lower right panels of Fig. 4 represent the transition between the regimes

where free-free and line-emission dominate. From the two upper panels, we see that $E_{p,\text{max}}$ reaches its maximum value at R_{dec} , and declines later. But this is not always the case; as shown in Appendix B, when the proton energy loss times are longer than the dynamical time, the maximum proton energy decreases throughout the evolution.

5 Expected neutrino emission from interaction-powered supernovae

In this section, the spectral energy distribution of neutrinos is introduced. We then present our findings on the dependence of the expected number of neutrinos on the SN model parameters and link the neutrino signal to the properties of the SN lightcurves.

5.1 Spectral energy distribution of neutrinos

A fraction ε_p of the dissipated kinetic energy of the shock (Eq. 13) is used to accelerate protons swept-up from the CSM; we adopt $\varepsilon_p = 0.1$, assuming that the shocks accelerating protons are parallel or quasi-parallel and therefore efficient diffusive shock acceleration occurs (Caprioli & Spitkovsky 2014). However, lower values of ε_p would be possible for oblique shocks, with poorer particle acceleration efficiency. Given the linear dependence of proton and neutrino spectra on this parameter, it is straightforward to rescale our results.

Assuming a power-law energy distribution with spectral index $k = 2$, the number of protons injected per unit radius and unit Lorentz factor is

$$Q_p(\gamma_p, R) = A(R) \gamma_p^{-2} \log^{-1} \left(\frac{\gamma_{p,\max}}{\gamma_{p,\min}} \right), \quad (17)$$

for $\gamma_{p,\min} < \gamma < \gamma_{p,\max}$, and zero otherwise. We set the minimum Lorentz factor of accelerated protons $\gamma_{p,\min} = 1$, while $\gamma_{p,\max}$ is obtained by comparing the acceleration and the energy-loss time scales at each radius during the shock evolution, as discussed in Sec. 4. The normalization factor $A(R)$ is

$$A(R) = \frac{9}{8} \pi \varepsilon_p R^2 v_{\text{sh}}^2(R) \rho_{\text{CSM}}(R) \propto \begin{cases} R^{\frac{2n-sn+5s-12}{n-3}} & \text{for } R \leq R_{\text{dec}} \\ R^{-1} & \text{for } R > R_{\text{dec}} \end{cases}. \quad (18)$$

The injection rate of protons in the deceleration phase does not depend on the SN density structure nor the CSM density profile. Since we aim to compute the neutrino emission, we track the temporal evolution of the proton distribution in the shocked region between the shock breakout radius R_{bo} and the outer radius R_{CSM} .

The evolution of the proton distribution is given by (Sturmer et al. 1997; Finke & Dermer 2012; Petropoulou et al. 2016):

$$\frac{\partial N_p(\gamma_p, R)}{\partial R} - \frac{\partial}{\partial \gamma_p} \left[\frac{\gamma_p}{R} N_p(\gamma_p, R) \right] + \frac{N_p(\gamma_p, R)}{v_{\text{sh}}(R) t_{\text{pp}}(R)} = Q_p(\gamma_p, R), \quad (19)$$

where $N_p(\gamma_p, R)$ represents the total number of protons in the shell at a given radius R with Lorentz factor between γ_p and $\gamma_p + d\gamma_p$. The second term on the left hand side of Eq. 19 takes into account energy losses due to the adiabatic expansion of the SN shell, while pp collisions are treated as an escape term (Sturmer et al. 1997). Other energy loss channels for protons are negligible (Murase et al. 2011). Furthermore, in Eq. 19, the diffusion term has been neglected since the shell is assumed to be homogeneous.

The neutrino production rates, $Q_{\nu_i + \bar{\nu}_i}$ [$\text{GeV}^{-1} \text{s}^{-1}$], for muon and electron flavor (anti)neutrinos are given by (Kelner et al. 2006):

$$Q_{\nu_\mu + \bar{\nu}_\mu}(E_\nu, R) = 4n_{\text{CSM}}(R) m_p c^3 \int_0^1 dx \frac{\sigma_{pp}(E_\nu/x)}{x} \times N_p \left(\frac{E_\nu}{x m_p c^2}, R \right) \left(F_{\nu_\mu}^{(1)}(E_\nu, x) + F_{\nu_\mu}^{(2)}(E_\nu, x) \right), \quad (20)$$

$$Q_{\nu_e + \bar{\nu}_e}(E_\nu, R) = 4n_{\text{CSM}}(R) m_p c^3 \int_0^1 dx \frac{\sigma_{pp}(E_\nu/x)}{x} \times N_p \left(\frac{E_\nu}{x m_p c^2}, R \right) F_{\nu_e}(E_\nu, x), \quad (21)$$

where $x = E_\nu/E_p$. The functions $F_{\nu_\mu}^{(1)}$, $F_{\nu_\mu}^{(2)}$ and F_{ν_e} follow the definitions in Kelner et al. (2006). Equations 20 and 21 are valid for $E_p > 0.1$ TeV, corresponding to the energy range under investigation. Note that, for the parameters we use in this work, the synchrotron

cooling of charged pions and muons produced via pp interactions is negligible. Therefore, the neutrino spectra are not affected by the cooling of mesons.

5.2 Energy emitted in neutrinos

The total energy that goes in neutrinos in the energy range $[E_{\nu,1}, E_{\nu,2}]$ during the entire interaction period is given by

$$\mathcal{E}_{\nu+\bar{\nu}} = \int_{t_{\text{BO}}}^{t_{\text{CSM}}} dt \int_{E_{\nu,1}}^{E_{\nu,2}} dE_\nu E_\nu [Q_{\nu_\mu + \bar{\nu}_\mu}(E_\nu, R) + Q_{\nu_e + \bar{\nu}_e}(E_\nu, R)], \quad (22)$$

where t_{BO} and t_{CSM} are expressed in the progenitor reference frame.

In order to connect the observed properties of the SN lightcurve to the neutrino ones (e.g., the total energy that goes in neutrinos or their typical spectral energy), for each configuration of SN model parameters we integrate the neutrino production rate between t_{BO} and t_{CSM} , for $E_\nu \geq 1$ TeV, as in Eq. 22. The results are shown in Fig. 5, where we fix two of the SN parameters at their benchmark values (see Table 1) and investigate $\mathcal{E}_{\nu+\bar{\nu}}$ in the plane spanned by the remaining two. Note that we do not consider the regions of the SN parameter space with the maximum achievable proton energy ($E_{p,\max}^*$, see Appendix B for more details) smaller than 10 TeV since they would lead to neutrinos in the energy range dominated by atmospheric events in IceCube (see Sec. 6). If we were to integrate the neutrino rate for $E_{\nu,1} > 1$ TeV (Eq. 22), the contour lines for $\mathcal{E}_{\nu+\bar{\nu}}$ would be shifted to the left. Isocontours of the maximum achievable proton energy $E_{p,\max}^*$ (first row), the rise time t_{rise} (second row), and the bolometric peak L_{peak} (third row) are also displayed on top of the $\mathcal{E}_{\nu+\bar{\nu}}$ colormap in Fig. 5.

In all panels of Fig. 5, $\mathcal{E}_{\nu+\bar{\nu}}$ increases with M_{CSM} , due to the larger target proton number. Nevertheless, such a trend saturates once the critical n_{CSM} (corresponding to a critical M_{CSM}) is reached, where either pp interactions or the cooling of thermal plasma significantly limit the maximum proton energy, thus decreasing the number of neutrinos produced with high energy. For masses larger than the critical CSM mass, neutrinos could be abundantly produced either appreciably increasing the kinetic energy (left panel), or decreasing the ejecta mass (middle panel), or increasing the CSM radius (right panel). From the contour lines in each panel, we see that the optimal configuration for what concerns neutrino production results from large E_k and small M_{ej} , which lead to large shock velocities v_{sh} , large R_{CSM} , and not extremely large M_{CSM} , compared to a fixed M_{ej} . Nevertheless, the panels in the upper row of Fig. 5 indicate that the configurations with the largest proton energies (and thus spectral neutrino energies) always prefer a balance between E_k , M_{ej} , and R_{CSM} with M_{CSM} .

It is important to observe the peculiar behavior resulting from the variation of R_{CSM} (right panels of Fig. 5). For fixed M_{CSM} , $\mathcal{E}_{\nu+\bar{\nu}}$ increases, then saturates at a certain R_{CSM} , and decreases thereafter. For very small R_{CSM} , the CSM density is relatively large, and the shock becomes collisionless close to R_{CSM} , probing a low fraction of the total CSM mass and thus producing a small number of neutrinos. This suppression is alleviated by increasing R_{CSM} . Nevertheless, a large R_{CSM} for fixed M_{CSM} leads to a low CSM density, and thus the total neutrino energy drops. For increasing M_{CSM} , such inversion in $\mathcal{E}_{\nu+\bar{\nu}}$ happens at larger R_{CSM} . We also see that the largest $\mathcal{E}_{\nu+\bar{\nu}}$ is obtained in the right upper corner of the right panels. This is mainly related to the duration of the shock interaction. The longer the interaction time, the larger the CSM mass swept-up by the collisionless shock.

The panels in the middle row of Fig. 5 show how the neutrino

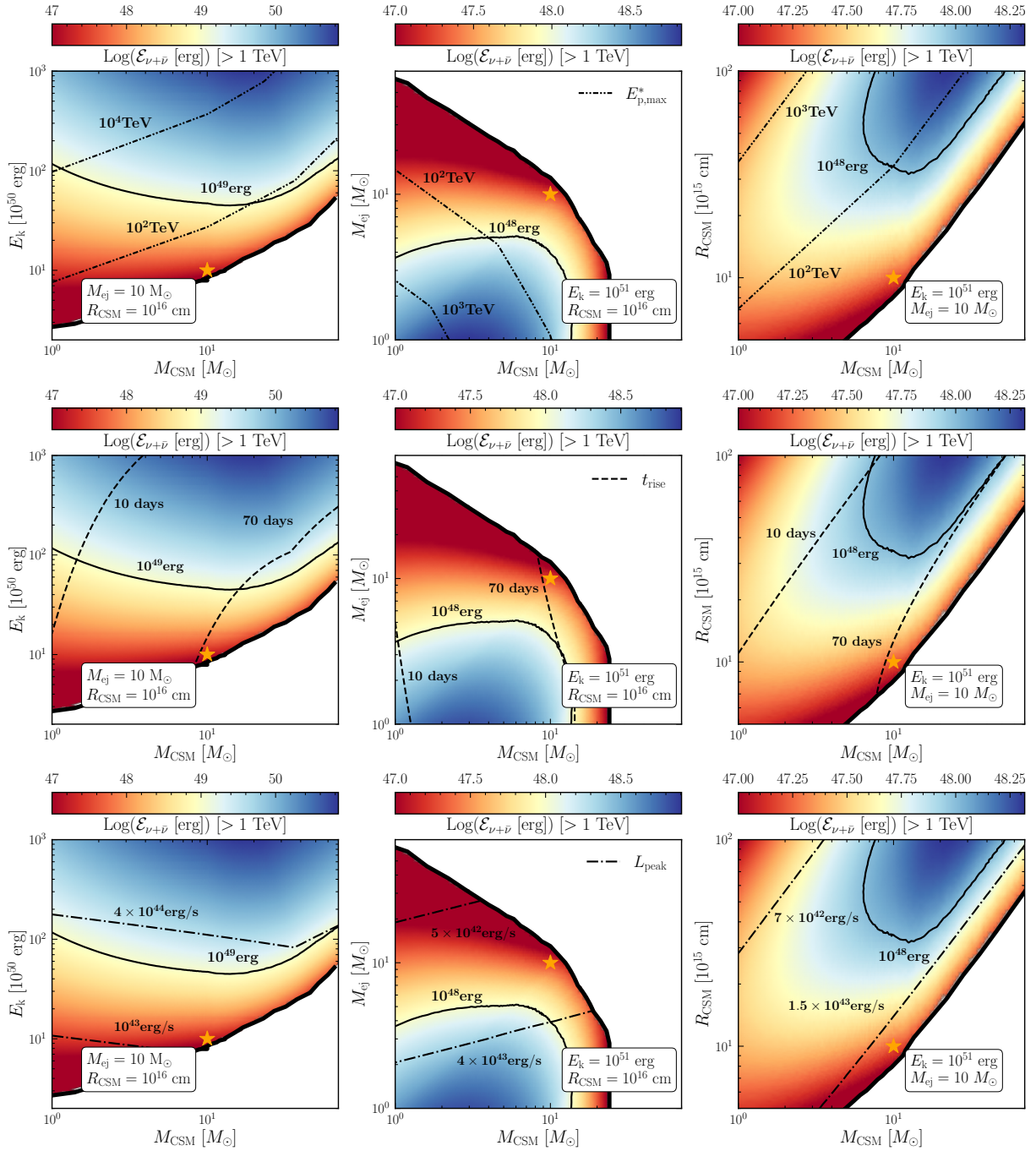


Figure 5. Contour plots of the total neutrino energy $\mathcal{E}_{\nu+\bar{\nu}}$ integrated for $E_{\nu} \geq 1$ TeV through the evolution of the shock in the CSM, as a function of M_{CSM} and E_k (left panels), M_{ej} (middle panels), and R_{CSM} (right panels) for the wind scenario. In order to highlight the dependence on the SN properties, isocontours of the maximum proton energy $E_{p,\text{max}}^*$ (double-dot dashed contours, top row), t_{rise} (dashed contours, middle row), and L_{peak} (dot dashed contours, bottom row) are displayed. All quantities are expressed in the SN reference frame. The white regions represent parts of the parameter space with $E_{p,\text{max}}^* \lesssim 10$ TeV excluded from our investigation. Our benchmark SN model is marked with an orange star. The SN configurations leading to the largest $\mathcal{E}_{\nu+\bar{\nu}}$ are given by large SN kinetic energies ($E_k \gtrsim 10^{51}$ erg), small ejecta masses ($M_{\text{ej}} \lesssim 10 M_{\odot}$), intermediate CSM masses with respect to M_{ej} (i.e., $1 M_{\odot} \lesssim M_{\text{CSM}} \lesssim 30 M_{\odot}$), and relatively large CSM extent ($R_{\text{CSM}} \gtrsim 10^{16}$ cm).

energy varies as a function of t_{rise} . Large neutrino energy is obtained for slow rising lightcurves. In particular, given our choice of the parameters for these contour plots, the most optimistic scenarios for neutrinos lie in the region with $10 \text{ days} \lesssim t_{\text{rise}} \lesssim 50 \text{ days}$. Such findings hold for a wide range of parameters for interacting SNe. Extremely large t_{rise} , on the other hand, are expected to be determined

by very large M_{CSM} , which can substantially limit the production of particles in the high energy regime.

The bottom panels of Fig. 5 illustrate how $\mathcal{E}_{\nu+\bar{\nu}}$ is linked to L_{peak} . In particular, L_{peak} closely tracks $\mathcal{E}_{\nu+\bar{\nu}}$. However, L_{peak} can increase with M_{CSM} to larger values than what neutrinos do, given its linear dependence on the CSM density (see Eq. 14). Overall, the regions

where the largest $\mathcal{E}_{\nu+\bar{\nu}}$ (and hence number of neutrinos) is obtained are also the regions where L_{peak} is the largest. It is not always true the opposite. Hence, large L_{peak} is a necessary, but not sufficient condition to have large $\mathcal{E}_{\nu+\bar{\nu}}$.

To summarize, a large $\mathcal{E}_{\nu+\bar{\nu}}$ is expected for large SN kinetic energy ($E_k \gtrsim 10^{51}$ erg), small ejecta mass ($M_{\text{ej}} \lesssim 10 M_{\odot}$), intermediate CSM mass with respect to M_{ej} ($1 M_{\odot} \lesssim M_{\text{CSM}} \lesssim 30 M_{\odot}$), and relatively extended CSM ($R_{\text{CSM}} \gtrsim 10^{16}$ cm). These features imply large bolometric luminosity peak ($L_{\text{peak}} \gtrsim 10^{43}\text{--}10^{44}$ erg) and average rise time ($t_{\text{rise}} \gtrsim 10\text{--}20$ days). On the other hand, it is important to note that degeneracies are present in the SN parameter space (see also Pitik et al. 2022) and comparable L_{peak} and t_{rise} can be obtained for SN model parameters (E_k , M_{ej} , R_{CSM} , and M_{ej}) that are not optimal for neutrino emission.

It is important to stress that in this section we have considered $\mathcal{E}_{\nu+\bar{\nu}}$ as a proxy of the expected number of neutrino events that is investigated in Sec. 6. Moreover, we have compared $\mathcal{E}_{\nu+\bar{\nu}}$ to the bolometric luminosity expected at the peak and not to the luminosity effectively radiated, $L_{\text{peak,obs}}$.

6 Neutrino detection prospects

In this section, we investigate the neutrino detection prospects. In order to do so, we select two especially bright SNe observed by ZTF, SN 2020usa and SN 2020in. On the basis of our findings, we also discuss the most promising strategies for neutrino searches and multi-messenger follow-up programs.

6.1 Expected number of neutrino events at Earth

The neutrino and antineutrino flux ($F_{\nu_{\alpha}+\bar{\nu}_{\alpha}}$ with $\alpha = e, \mu, \tau$) at Earth from a SN at redshift z and as a function of time in the observer frame is [$\text{GeV}^{-1}\text{s}^{-1}\text{cm}^{-2}$]:

$$F_{\nu_{\alpha}+\bar{\nu}_{\alpha}}(E_{\nu}, t) = \frac{(1+z)^2}{4\pi d_L^2(z)} v_{\text{sh}} \sum_{\beta} P_{\nu_{\beta} \rightarrow \nu_{\alpha}} Q_{\nu_{\beta}+\bar{\nu}_{\beta}} \left(E_{\nu_{\alpha}}(1+z), \frac{v_{\text{sh}} t}{1+z} \right), \quad (23)$$

where $Q_{\nu_{\beta}+\bar{\nu}_{\beta}}$ is defined as in Eqs. 20 and 21. Neutrinos change their flavor while propagating, hence the flavor transition probabilities are given by (Anchordoqui et al. 2014):

$$P_{\nu_e \rightarrow \nu_{\mu}} = P_{\nu_{\mu} \rightarrow \nu_e} = P_{\nu_e \rightarrow \nu_{\tau}} = \frac{1}{4} \sin^2 2\theta_{12}, \quad (24)$$

$$P_{\nu_{\mu} \rightarrow \nu_{\mu}} = P_{\nu_{\mu} \rightarrow \nu_{\tau}} = \frac{1}{8} (4 - \sin^2 2\theta_{12}), \quad (25)$$

$$P_{\nu_e \rightarrow \nu_e} = 1 - \frac{1}{2} \sin^2 2\theta_{12}, \quad (26)$$

with $\theta_{12} \simeq 33.5$ deg (Esteban et al. 2020), and $P_{\nu_{\beta} \rightarrow \nu_{\alpha}} = P_{\bar{\nu}_{\beta} \rightarrow \bar{\nu}_{\alpha}}$. The luminosity distance $d_L(z)$ is defined in a flat Λ CDM cosmology:

$$d_L(z) = (1+z) \frac{c}{H_0} \int_0^z \frac{dz'}{\sqrt{\Omega_{\Lambda} + \Omega_M(1+z')^3}}, \quad (27)$$

where $\Omega_M = 0.315$, $\Omega_{\Lambda} = 0.685$ and the Hubble constant is $H_0 = 67.4 \text{ km s}^{-1} \text{ Mpc}^{-1}$ (Aghanim et al. 2020).

Due to the better angular resolution of muon-induced track events compared to cascades, we focus on muon neutrinos and antineutrinos. Therefore, the event rate expected at the IceCube Neutrino Observatory, after taking into account neutrino flavor conversion, is

$$\dot{N}_{\nu_{\mu}+\bar{\nu}_{\mu}} = \int_{E_{\nu,1}}^{E_{\nu,2}} dE_{\nu} A_{\text{eff}}(E_{\nu}, \alpha) F_{\nu_{\mu}+\bar{\nu}_{\mu}}(E_{\nu}, t), \quad (28)$$

where $A_{\text{eff}}(E_{\nu}, \alpha)$ is the detector effective area (IceCube Collaboration et al. 2021) for a SN at declination α .

6.2 Expected number of neutrino events for SN 2020usa and SN 2020in

To investigate the expected number of neutrino events, we select two among the brightest sources observed by ZTF whose observable properties are summarized in Table 2: SN2020usa** and SN2020in††. We retrieve the photometry data of the sources in the ZTF-g and ZTF-r bands, and correct the measured fluxes for Galactic extinction (Schlafly & Finkbeiner 2011). Using linear interpolation of the individual ZTF-r and ZTF-g light curves, we perform a trapezoid integration between the respective center wavelengths to estimate the radiated energy at each time of measurement. The resulting lightcurve is interpolated with Gaussian process regression (Ambikasaran et al. 2015) and taken as a lower limit to the bolometric SN emission. From such pseudo-bolometric lightcurve, the rise time and peak luminosity are determined. The rise time is defined as the difference between the peak time and the estimated SN breakout time. The latter is determined by taking the average between the time of the first detection in ZTF-g or ZTF-r bands and the last non-detection in either band. In what follows, we consider the radiative efficiency $\varepsilon_{\text{rad}} = L_{\text{peak,obs}}/L_{\text{peak}}$ as a free parameter in the range $\varepsilon_{\text{rad}} \in [0.2, 0.7]$ (see, e.g., Villar et al. 2017). Furthermore, we assume that $\varepsilon_{\text{rad}} = E_{\text{rad,obs}}/E_{\text{diss,thick}}$ also holds.

For both SNe, we perform a scan over the SN model parameters (E_k , M_{ej} , M_{CSM} , and R_{CSM}) which fulfill the following conditions:

- $t_{\text{rise}} \in [1, 1.5] \times t_{\text{rise,obs}}$, namely we allow an error up to 50% on the estimation of t_{rise} ;
- $L_{\text{peak}} \geq L_{\text{peak,obs}}$;
- $E_k > E_{\text{rad,obs}}$. We narrow the investigation range to $E_k \in [10^{51}, 2 \times 10^{52}]$ erg for SN2020usa and $E_k \in [4 \times 10^{50}, 5 \times 10^{51}]$ erg for SN2020in, assuming that at least $\sim 10\%$ and at most 80% of the total energy E_k is radiated.
- $t_{\text{dur,th}} \geq t_{\text{dur,obs}}$. Here $t_{\text{dur,obs}}$ is the observational temporal window available for each SN event, while $t_{\text{dur,th}} = t(R_{\text{ph}}) - t(R_{\text{bo}})$ is the time that the shock takes to cross the optically thick part of the CSM envelope after breakout (as mentioned in Sec. 2.3, the shock is expected to peak in the X-ray band once out of the optically thick part).

Figure 6 shows the total number of muon neutrino and antineutrino events, integrated over the duration of the interaction in the CSM for $E_{\nu} \geq 1$ TeV, expected at IceCube in the the wind scenario, for E_k selected to maximize the space of parameters compatible with the conditions mentioned above. Similarly to Fig. 5, the regions with the largest number of neutrino events are those with lower M_{ej} and larger R_{CSM} , for fixed M_{CSM} . It is important to note that, for given observed SN properties ($L_{\text{peak,obs}}$ and $t_{\text{rise,obs}}$), the expected number of neutrino events is not unique; in fact, as shown in Sec. 5, there is degeneracy in the SN model parameters that leads to the same $L_{\text{peak,obs}}$ and $t_{\text{rise,obs}}$.

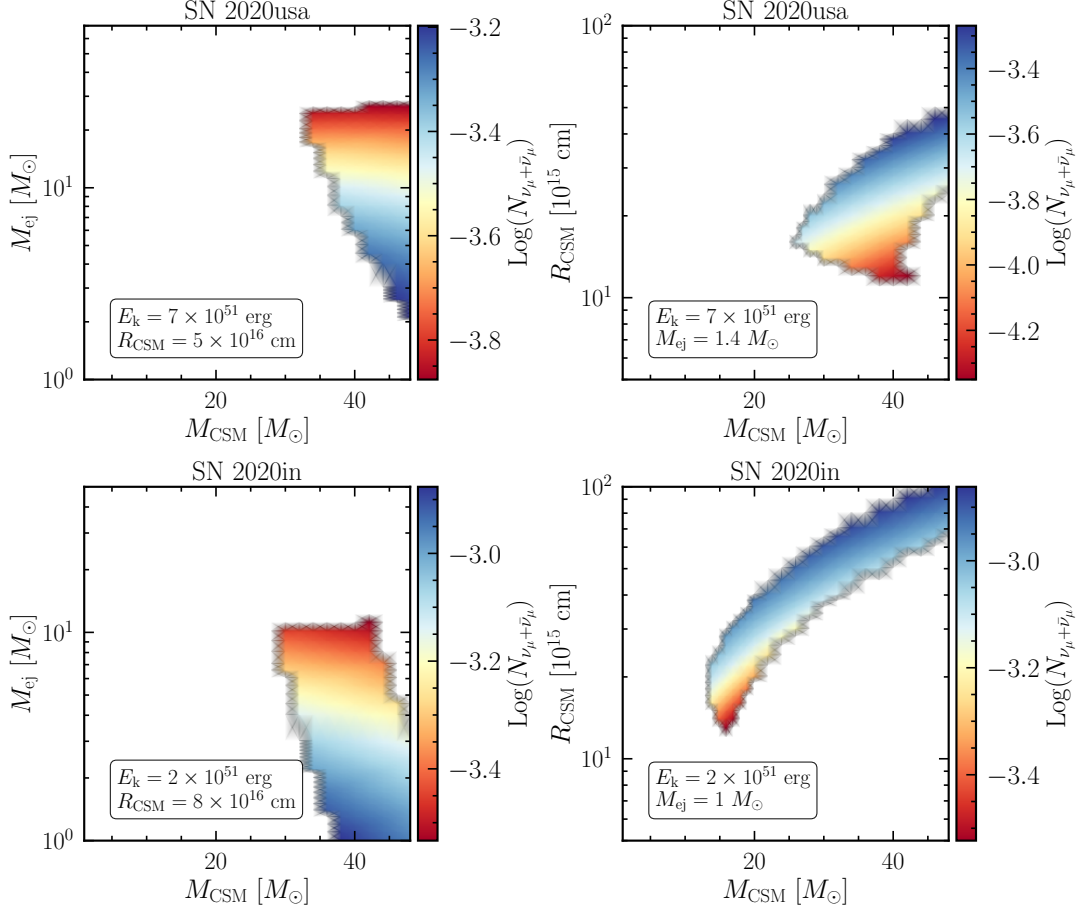
Figure 7 represents the muon neutrino and antineutrino event rate expected at IceCube for SN2020usa and SN2020in, each as a function of time for two energy ranges, and for the most optimistic scenario. Figure 8 displays the corresponding cumulative neutrino

** <https://lasair-ztf.lsst.ac.uk/objects/ZTF20acbcfaa/>

†† <https://lasair-ztf.lsst.ac.uk/objects/ZTF20aaaweke/>

Table 2. Characteristic properties of our representative SLSNe, SN 2020usa and SN 2020in.

	Redshift	$t_{\text{rise,obs}}$ [days]	$L_{\text{peak,obs}}$ [erg s $^{-1}$]	$E_{\text{rad,obs}}$ [erg]	$t_{\text{dur,obs}}$ [days]	Declination [deg]
SN 2020usa	0.26	65	8×10^{43}	1.3×10^{51}	350	-2.3
SN 2020in	0.11	42	3×10^{43}	3.3×10^{50}	413	20.2


Figure 6. Contour plot of the number of muon neutrino and antineutrino events expected at the IceCube Neutrino Observatory (for the wind scenario and integrated over the duration of CSM interaction) in the SN model parameter space compatible with the observation of SN2020usa (top panels) and SN2020in (bottom panels). Only a fraction of the SN parameter space is compatible with the optical data. Importantly, for fixed $L_{\text{peak,obs}}$ and $t_{\text{rise,obs}}$, a different number of neutrino events could be obtained according to the specific combination of M_{ej} , M_{CSM} , R_{CSM} , E_k compatible with the observed optical properties.

number of events for both most optimistic and pessimistic scenarios. The two cases are selected after scanning over ε_{rad} . The smaller is ε_{rad} , the higher E_k is needed to explain the observations, and since we adopt a fixed fraction of the shock energy ε_p that goes into acceleration of relativistic protons, the best case for neutrino production is the one with the lowest ε_{rad} . Choosing $\varepsilon_{\text{rad,min}} = 0.2$, we only select the SN parameters that satisfy the following conditions: $t_{\text{rise}} \in [1, 1.5] \times t_{\text{rise,obs}}$, $L_{\text{peak}} \in [1, 1.5] \times L_{\text{peak,obs}}/\varepsilon_{\text{rad,min}}$, and $E_{\text{rad}} \in [1, 1.5] \times E_{\text{rad,obs}}/\varepsilon_{\text{rad,min}}$, hence considering an error on $L_{\text{peak,obs}}$ and $E_{\text{rad,obs}}$ of at most 50%. After an initial rise, the neutrino event rate for both considered energy ranges (100 GeV–100 TeV and 100 TeV–1 PeV) decreases with time, with a steeper rate for the high-energy range, where the slow increase of $E_{p,\text{max}}$ does not compensate the drop in the CSM density. Note that the cumulative number of neutrino events is relatively small because, although the SN 2020usa and SN 2020in have large $L_{\text{peak,obs}}$, they occurred at relatively large distance from Earth (\sim Gpc), as evident

from Table 2. If other SNe exhibiting similar photometric properties should be observed at smaller z , then the expected neutrino flux should be rescaled with respect to the results shown here by the SN distance squared (see Sec. 6.4 and Fig. 10).

Figure 9 shows, for the most optimistic SN model parameter configuration, a comparison between $L_{\nu_\mu + \bar{\nu}_\mu}$ (obtained taking into account flavor oscillation) and the optical luminosity for SN 2020usa and SN 2020in. Besides the difference in the intrinsic optical brightness, the two SNe display comparable evolution in the neutrino luminosity, with the neutrino luminosity peak being ~ 3 times brighter for SN 2020usa than SN 2020in. This is due to the fact that t_{rise} and L_{peak} for both SNe are such to lead to similar SN model parameters for what concerns the most optimistic prospects for neutrino emission. Note that an investigation that also takes into account the late evolution of the optical lightcurve might have an impact on this result, but it out of the scope of this work.

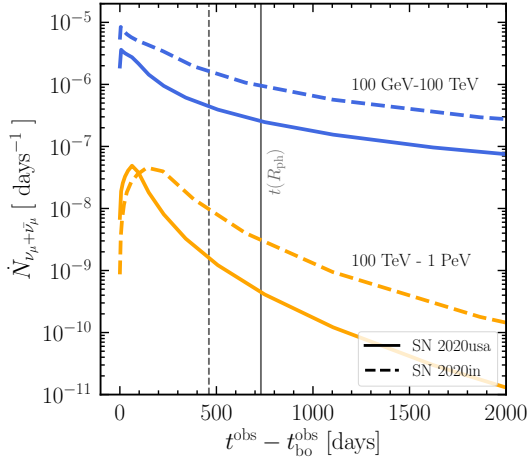


Figure 7. Muon neutrino and antineutrino event rates predicted for SN 2020usa and SN 2020in at the IceCube Neutrino Observatory as functions of time in the observer frame, after the shock breakout, assuming $\epsilon_{\text{rad}} = 0.2$. The SN model parameters have been chosen to optimize neutrino production [$M_{\text{ej}} = 5.5 M_{\odot}$, $M_{\text{CSM}} = 48 M_{\odot}$, $R_{\text{CSM}} = 5.5 \times 10^{16}$ cm, $E_k = 10^{52}$ erg for SN2020usa; $M_{\text{ej}} = 5 M_{\odot}$, $M_{\text{CSM}} = 46 M_{\odot}$, $R_{\text{CSM}} = 10^{17}$ cm, $E_k = 5 \times 10^{51}$ erg for SN2020in]. The event rate increases slightly more slowly in the high energy band (100 TeV–1 PeV) with respect to the low energy one at early times, and it declines after peak because of the decreasing trend of v_{sh} as a function of time. The gray vertical lines indicate the time at which the shock reaches the photospheric radius R_{ph} (solid and dashed for SN 2020 usa and SN 2020in, respectively).

6.3 Characteristics of the detectable neutrino signal

The neutrino luminosity curve does not peak at the same time as the optical lightcurve, as visible from Fig. 9. In fact the position of the optical peak is intrinsically related to propagation effects of photons in the CSM, and thus to the CSM properties, as discussed in Sec. 3 and Appendix A. The peak in the neutrino curve, instead, solely depends on the CSM radial density distribution and the evolution of the maximum spectral energy. Because of this, the neutrino event rate as well as the neutrino luminosity in the high-energy range (100 TeV–1 PeV) peak at $t|_{E_{\text{p,max}}^*}$, namely the time at which the maximum proton energy is reached (see Appendix B for $E_{\text{p,max}}$ and Fig. 11 for the trend of the neutrino flux at Earth).

The most favorable time window for detecting energetic neutrinos ($\gtrsim 100$ TeV) would be a few times t_{rise} around the electromagnetic bolometric peak, which corresponds to $\mathcal{O}(100 \text{ days})$ days for $E_k \lesssim 10^{52}$ erg, $M_{\text{ej}} \lesssim 10 M_{\odot}$, $M_{\text{CSM}} \lesssim 20 M_{\odot}$, and $R_{\text{CSM}} \lesssim \text{few} \times 10^{16}$ cm (see Fig. B1). Interestingly, the IceCube neutrino event IC200530A associated with the candidate SLSN event AT2019fdr was detected about 300 days after the optical peak (Pitik et al. 2022), in agreement with our findings $\ddagger\ddagger$.

Figure 10 shows the dependence of the number of neutrino events expected in IceCube and IceCube-Gen2 in a temporal window of 200 days and as functions of the redshift for a benchmark SN with the same properties of SN 2020usa, but placed at declination $\alpha = 0$ deg and redshift z . We consider the number of neutrino events expected in a time window of 200 days in order to optimize the signal over

$\ddagger\ddagger$ AT2019fdr occurred at $z \approx 0.27$, and the optical lightcurve displayed $t_{\text{rise}} = 98$ days and $L_{\text{peak}} = 2.1 \times 10^{44}$ erg/s, considering a radiative efficiency of 18–35%, Pitik et al. (2022) estimated that about 4.6×10^{-2} muon neutrino and antineutrino events were expected assuming excellent discrimination of the atmospheric background.

background classification (see Sec. 6.5). One can see that IceCube expects to detect $N_{\nu_\mu + \bar{\nu}_\mu} \gtrsim 10$ for SNe at distance $\lesssim 9$ Mpc ($z \lesssim 0.002$); while $N_{\nu_\mu + \bar{\nu}_\mu} \gtrsim 10$ should be detected for SNe at a distance $\lesssim 13$ Mpc ($z \lesssim 0.003$) for IceCube-Gen2 (Aartsen et al. 2021).

In order to compare the expected number of neutrino events with the likelihood of finding SNe at redshift z , Fig. 10 also shows the core-collapse SN rate (Yuksel et al. 2008; Vitagliano et al. 2020) for reference. Note that the rate of interaction-powered SNe is very uncertain and it is not clear whether their redshift evolution follows the star-formation rate (Smith et al. 2011); hence the core-collapse SN rate should be considered as an upper limit of the rate of interaction-powered SNe and SLSNe, under the assumption that the latter follow the same redshift evolution.

The evolution of the energy flux of neutrinos is displayed in Fig. 11. One can see that for $E_\nu \gtrsim 100$ TeV, the energy flux increases up to around 100 days, and then decreases. This trend can be explained considering the evolution of $E_{\text{p,max}}$ (see also Fig. 9).

6.4 Follow-up strategy for neutrino searches

Our findings in Sec. 5.1 suggest that a large L_{peak} and average t_{rise} are necessary, but not sufficient, to guarantee large neutrino emission. This is due to the large degeneracy existing in the SN model parameter space that could lead to SN lightcurves with comparable properties in the optical, but largely different neutrino emission.

Despite the degeneracy in the SN properties leading to comparable optical signals, the semi-analytical procedure outlined in this work allows to restrict the range of E_k , M_{ej} , M_{CSM} , and R_{CSM} that matches the measured t_{rise} and L_{peak} . This procedure then forecasts an expectation range for the number of neutrino events detectable by IceCube to guide upcoming follow-up searches (see Sec. 6.2 for an application to two SNe detected by ZTF), also taking into account the unknown radiative efficiency ϵ_{rad} .

For measured t_{rise} and L_{peak} , through the method outlined in this paper, it is possible to predict the largest expected number of neutrino events. On the other hand, if an interaction-powered SN should be detected in the optical, and no neutrino should be observed, this would imply that the SN model parameters compatible with the measured t_{rise} and L_{peak} are not optimal for neutrino production.

Our findings highlight the need to carry out multi-wavelength SN observations to better infer the SN properties and then optimize neutrino searches through the procedure presented in this work. In fact, relying on radio and X-ray all-sky surveys, one could narrow down the values of M_{ej} , M_{CSM} , and R_{CSM} compatible with the data (Margalit et al. 2022; Chevalier & Fransson 2017). Because CSM interaction signatures appear clearly in the UV, early SN observations by future ultraviolet satellites, such as ULTRASAT (Shvartzvald et al. 2023), will be critical to provide insights into the CSM properties. Further information on the CSM can be obtained in the X-ray regime (Margalit et al. 2022), e.g. through surveys such as the extended ROentgen Survey with an Imaging Telescope Array (eROSITA; Predehl et al. 2010). In addition, the Vera Rubin Observatory (LSST Science Collaboration et al. 2009) will detect numerous SNe providing a large sample for a neutrino stacking analysis.

6.5 Multi-messenger follow-up programs

There are two ways to search for neutrinos from SNe.

- One can compile a catalog of SNe detected by electromagnetic surveys and use archival all-sky neutrino data to search for an excess of neutrinos from the catalogued sources. Such a search is most

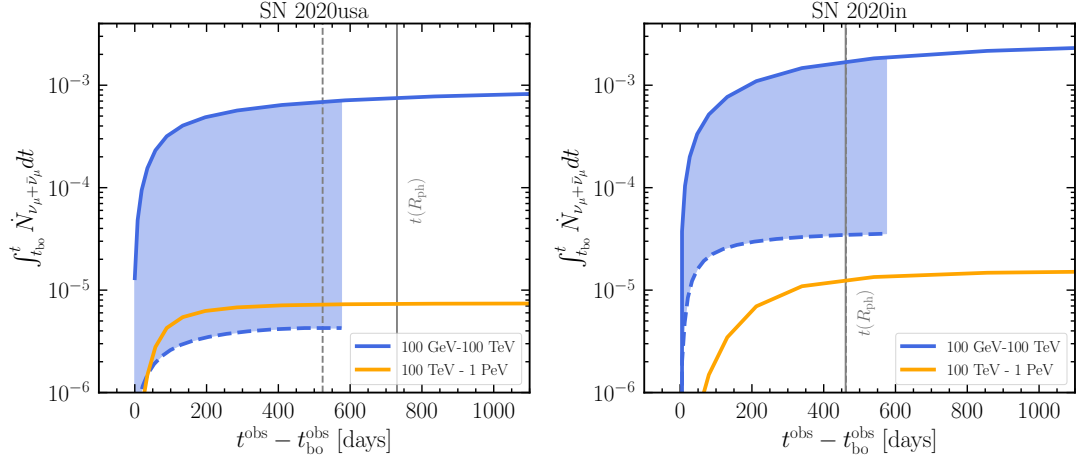


Figure 8. Cumulative number of muon neutrino and antineutrino events for SN 2020usa and SN2020in, as functions of time in the observer frame. The solid and dashed lines correspond to the most optimistic and pessimistic cumulative number of events in the indicated energy range, respectively. The SN model parameters for the most optimistic scenario are the same as the ones in Fig. 7, while the parameters leading to the most pessimistic conditions for neutrino production are $M_{\text{ej}} = 1 M_{\odot}$, $M_{\text{CSM}} = 25 M_{\odot}$, $R_{\text{CSM}} = 9 \times 10^{15}$ cm, $E_k = 2 \times 10^{51}$ erg for SN 2020usa, and $M_{\text{ej}} = 1.6 M_{\odot}$, $M_{\text{CSM}} = 10 M_{\odot}$, $R_{\text{CSM}} = 9 \times 10^{15}$ cm, $E_k = 7 \times 10^{50}$ erg, for SN2020in. In both cases $\varepsilon_{\text{rad}} = 0.7$. Neutrinos in the energy range [100 TeV, 1 PeV] are not produced in the pessimistic scenarios. The gray vertical lines indicate the time at which the shock reaches the photospheric radius R_{ph} .

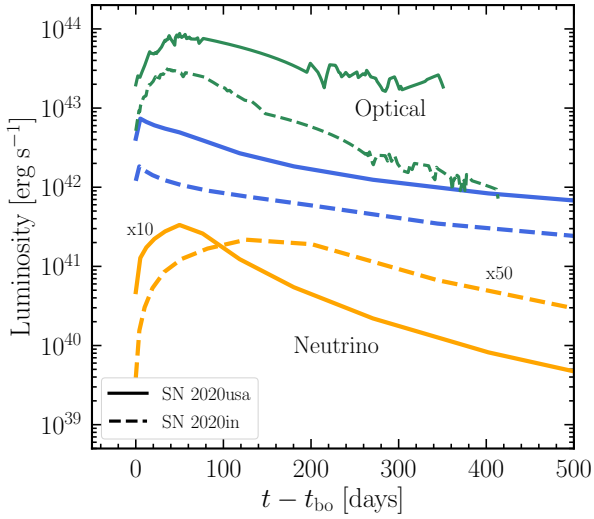


Figure 9. Muon neutrino and antineutrino (taking into account flavor oscillation, in blue and orange) and optical luminosities (after interpolation, in green) for SN 2020usa (solid lines) and SN 2020in (dashed lines) as functions of time in the source frame. The two selected SNe exhibit a comparable evolution of the total neutrino luminosity (blue lines) because t_{rise} and L_{peak} for both SNe are such to lead to similar parameters for what concerns the most optimistic prospects for neutrino emission. The blue curves have been obtained by considering the 100 GeV–1 PeV energy range. The orange lines represent the neutrino luminosity in the high energy range 100 TeV–1 PeV and show how the peak of the high energy neutrinos is shifted [up to $O(100)$ days] with respect to the optical peak.

sensitive when a stacking of all sources is applied (see e.g. Abbasi et al. 2023). The stacking requires a weighting of the sources relative to each other. Previous searches assumed that all sources are neutrino standard candles, i.e. the neutrino flux at Earth would scale with the inverse of the square of the luminosity distance, or used the optical peak flux as a weight. This work indicates that neither of those assumptions is justified. Modeling of the multi-wavelength emission

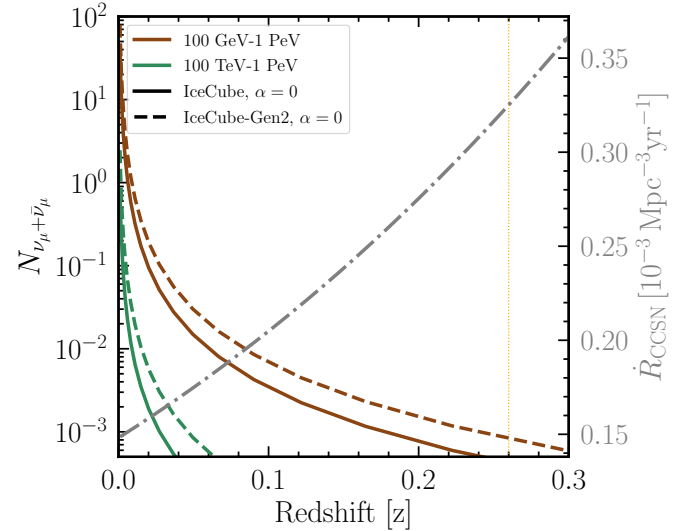


Figure 10. Number of muon neutrino and antineutrino events expected at the IceCube Neutrino Observatory (solid lines) and IceCube Gen2 (dashed lines) as functions of the redshift for a benchmark SN with the same properties of SN 2020usa but located at declination $\alpha = 0$ and variable z . The number of neutrino events is obtained integrating up to 200 days to optimize the signal discrimination with respect to the background. The redshift of SN 2020usa is marked with a dashed orange line to guide the eye. The core-collapse SN rate is plotted as a dot-dashed line (see y-axis scale on the right), in order to compare the expected number of neutrino events with the probability of finding SNe at a given z ; the core-collapse SNe rate should be considered as an upper limit of the rate of interaction-powered SNe and SLSNe (see main text for details). We expect $N_{\nu_\mu + \bar{\nu}_\mu} = 10$ at $z \approx 0.002$ ($d_L \geq 9$ Mpc) for IceCube and $z \approx 0.003$ ($d_L \geq 13$ Mpc) for IceCube-Gen2.

can yield a source-by-source prediction of the neutrino emission, which can be used as a weight.

Another important analysis choice is the time window to consider for the neutrino search. A too long time window increases the back-

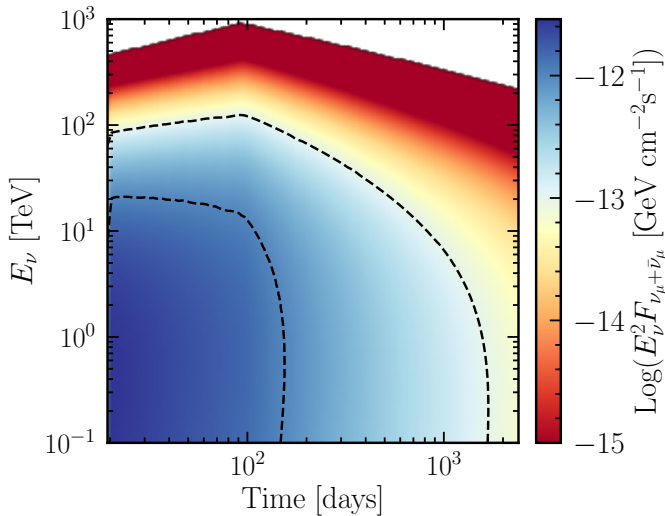


Figure 11. Contour plot of the muon neutrino and antineutrino energy flux expected at Earth for SN2020usa in the best case scenario and in the plane spanned by the arrival time of neutrinos and the neutrino energy. At low energies the neutrino flux decreases with time after the breakout. At high energies ($E_\nu \gtrsim 100$ TeV), instead, it increases with time, peaks at around 100 days, and then decreases. This is related to the time of maximum $E_{p,\max}$ (see also Fig. 9). The white color marks the regions where the flux is zero.

ground of atmospheric neutrinos, while a too short time window cuts parts of the signal. The prediction of the temporal evolution of the neutrino signal by our modeling allows to optimize the neutrino search time window. Finally, also the spectral energy distribution of neutrinos from SNe can be used to optimize the analysis in terms of background rejection.

- One can utilize electromagnetic follow-up observations of neutrino alerts released by neutrino telescopes (see e.g., [Aartsen et al. 2017](#)). Also here, defining a time window in order to assess the coincidence between an electromagnetic counterpart and the neutrino alert will be crucial. Once a potential counterpart is identified further follow-up observations (e.g. spectroscopy and multiple wavelength) can be scheduled to ensure classification of the source as SN and allow for a characterization of the CSM properties.

In order to forecast the expected neutrino signal reliably and better guide neutrino searches, in addition to optical data, input from X-ray and radio surveys would allow to characterize the CSM properties (see Sec. 6.4). In addition, it would be helpful to guide neutrino searches relying on the optical spectra at different times to characterize the duration of the interaction.

In summary, the modeling of particle emission from SNe presented in this paper will be crucial to guide targeted multi-messenger searches.

7 Conclusions

Supernovae and SLSNe of Type II_n show in their spectra strong signs of circumstellar interaction with a hydrogen-rich medium. The interaction between the SN ejecta and the CSM powers thermal UV/optical emission as well as high-energy neutrino emission. This work aims to explore the connection between the energy emitted in neutrinos detectable at the IceCube Neutrino Observatory (and its successor IceCube-Gen2) and the photometric properties of the optical signals observable by wide-field, high-cadence surveys. Our

main goal is to outline the best follow-up strategy for upcoming multi-messenger searches.

We rely on a semi-analytical model that connects the optical lightcurve observables to the SN properties and the correspondent neutrino emission, we find that the largest energy emitted in neutrinos and antineutrino is expected for large SN kinetic energy ($E_k \gtrsim 10^{51}$ erg), small ejecta mass ($M_{\text{ej}} \lesssim 10 M_\odot$), intermediate CSM mass ($1 M_\odot \lesssim M_{\text{CSM}} \lesssim 30 M_\odot$), and extended CSM ($R_{\text{CSM}} \gtrsim 10^{16}$ cm). Such parameters lead to large bolometric peak luminosity ($L_{\text{peak}} \gtrsim 10^{43}$ – 10^{44} erg) and average rise time ($t_{\text{rise}} \gtrsim 10$ – 40 days). However, these lightcurve features are necessary but not sufficient to guarantee ideal conditions for neutrino detection. In fact, different configurations of the SN model parameters could lead to comparable optical lightcurves, but vastly different neutrino emission.

The degeneracy between the optical lightcurve properties and the SN model parameters challenges the possibility of outlining a simple procedure to determine the expected number of IceCube neutrino events by solely relying on SN observations in the optical. While our method allows to foresee the largest possible number of neutrino events for given L_{peak} and t_{rise} , the eventual lack of neutrino detection for upcoming nearby SNe could hint towards SN properties that are different with respect to the ones maximizing the neutrino signal, therefore constraining the SN model parameter space compatible with neutrino and optical observations.

We also find that the peak of the neutrino curve does not coincide with the one of the optical lightcurve. Hence, one should consider a time window of a few t_{rise} around L_{peak} when looking for neutrinos. The time window should indeed be optimized to guarantee a fair signal discrimination with respect to the background.

Our findings suggest that previous neutrino stacking searches that assumed all SNe as neutrino standard candles, or used weights based on optical peak flux, might have not been optimal, as they do not take into account the diversity in the SN properties leading to a large variation in the number of neutrinos expected at Earth. Importantly, multi-wavelength observations are necessary to break the degeneracy between the optical lightcurve and the SN properties and will be essential to forecast the expected neutrino signal and optimize multi-messenger searches.

Acknowledgments

We are grateful to Takashi Moriya for insightful discussions, Steve Schulze for discussions on the ZTF lightcurve data, and Jakob van Santen for exchanges concerning the IceCube-Gen2 effective areas. We acknowledge support from the Villum Foundation (Project No. 13164), the Carlsberg Foundation (CF18-0183), as well as the Deutsche Forschungsgemeinschaft through Sonderforschungsbereich SFB 1258 “Neutrinos and Dark Matter in Astro- and Particle Physics” (NDM) and the Collaborative Research Center SFB 1491 “Cosmic Interacting Matters - from Source to Signal.” T.P. also acknowledges support from Fondo Ricerca di Base 2020 (MOSAICO) of the University of Perugia.

Data Availability

Data can be shared upon reasonable request to the authors.

REFERENCES

- Aartsen M. G., et al., 2017, *Astropart. Phys.*, 92, 30
- Aartsen M. G., et al., 2021, *J. Phys. G*, 48, 060501
- Abbasi R., et al., 2021a, *Phys. Rev. D*, 104, 022002
- Abbasi R., et al., 2021b, *Astrophys. J.*, 910, 4
- Abbasi R., et al., 2023, *Astrophys. J. Lett.*, 949, L12
- Aghanim N., et al., 2020, *Astron. Astrophys.*, 641, A6
- Ahlers M., Halzen F., 2018, *Prog. Part. Nucl. Phys.*, 102, 73
- Ambikasaran S., Foreman-Mackey D., Greengard L., Hogg D. W., O’Neil M., 2015, *IEEE Transactions on Pattern Analysis and Machine Intelligence*, 38, 252
- Anchordoqui L. A., et al., 2014, *JHEAp*, 1-2, 1
- Bell A. R., 2004, *Mon. Not. Roy. Astron. Soc.*, 353, 550
- Bell A. R., 2013, *Astropart. Phys.*, 43, 56
- Bellm E. C., et al., 2019, *PASP*, 131, 018002
- Blasi P., 2013, *Astron. Astrophys. Rev.*, 21, 70
- Blinnikov S., 2017, in Alsabti A. W., Murdin P., eds., *Handbook of Supernovae*. p. 843, doi:10.1007/978-3-319-21846-5_31
- Brose R., Sushch I., Mackey J., 2022, *Mon. Not. Roy. Astron. Soc.*, 516, 492
- Caprioli D., Spitkovsky A., 2014, *Astrophys. J.*, 783, 91
- Cardillo M., Amato E., Blasi P., 2015, *Astropart. Phys.*, 69, 1
- Chambers K. C., et al., 2016, *arXiv e-prints*, p. arXiv:1612.05560
- Chatzopoulos E., Wheeler J. C., Vinko J., 2012, *Astrophys. J.*, 746, 121
- Chatzopoulos E., Wheeler J. C., Vinko J., Horvath Z. L., Nagy A., 2013, *Astrophys. J.*, 773, 76
- Chevalier R. A., 1982, *ApJ*, 259, 302
- Chevalier R. A., Fransson C., 1994, *Astrophys. J.*, 420, 268
- Chevalier R. A., Fransson C., 2017, in Alsabti A. W., Murdin P., eds., *Handbook of Supernovae*. p. 875, doi:10.1007/978-3-319-21846-5_34
- Chevalier R. A., Irwin C. M., 2011, *Astrophys. J. Lett.*, 729, L6
- Cristofari P., 2021, *Universe*, 7, 324
- Cristofari P., Blasi P., Amato E., 2020, *Astropart. Phys.*, 123, 102492
- Dekany R., et al., 2020, *PASP*, 132, 038001
- Draine B. T., 2011, *Physics of the Interstellar and Intergalactic Medium*
- Drake A. J., et al., 2011, *Astrophys. J.*, 735, 106
- Ellison D. C., Patnaude D. J., Slane P., Blasi P., Gabici S., 2007, *Astrophys. J.*, 661, 879
- Esteban I., Gonzalez-Garcia M., Maltoni M., Schwetz T., Zhou A., 2020, *JHEP*, 09, 178
- Fang K., Metzger B. D., Vurm I., Aydi E., Chomiuk L., 2020, *Astrophys. J.*, 904, 4
- Filippenko A. V., 1997, *Ann. Rev. Astron. Astrophys.*, 35, 309
- Finke J. D., Dermer C. D., 2012, *Astrophys. J.*, 751, 65
- Gal-Yam A., 2012, *Science*, 337, 927
- Gal-Yam A., 2017, in Alsabti A. W., Murdin P., eds., *Handbook of Supernovae*. p. 195, doi:10.1007/978-3-319-21846-5_35
- Gal-Yam A., 2019, *Ann. Rev. Astron. Astrophys.*, 57, 305
- Gal-Yam A., et al., 2007, *Astrophys. J.*, 656, 372
- Ginzburg S., Balberg S., 2012, *Astrophys. J.*, 757, 178
- Halzen F., Kheirandish A., 2022, *arXiv e-prints*, p. arXiv:2202.00694
- Hambleton K. M., et al., 2022, *arXiv e-prints*, p. arXiv:2208.04499
- IceCube Collaboration et al., 2021, *arXiv e-prints*, p. arXiv:2101.09836
- Kankare E., et al., 2019, *Astron. Astrophys.*, 626, A117
- Katz B., Sapir N., Waxman E., 2011, *arXiv e-prints*, p. arXiv:1106.1898
- Kelner S. R., Aharonian F. A., Bugayov V. V., 2006, *Phys. Rev. D*, 74, 034018
- Kheirandish A., Murase K., 2022, *arXiv e-prints*, p. arXiv:2204.08518
- Kochanek C. S., et al., 2017, *PASP*, 129, 104502
- LSST Science Collaboration et al., 2009, *arXiv e-prints*, p. arXiv:0912.0201
- Levinson A., Bromberg O., 2008, *Phys. Rev. Lett.*, 100, 131101
- Lodders K., 2019, *arXiv e-prints*, p. arXiv:1912.00844
- Margalit B., Quataert E., Ho A. Y. Q., 2022, *Astrophys. J.*, 928, 122
- Matzner C. D., McKee C. F., 1999, *Astrophys. J.*, 510, 379
- Mészáros P., 2017, *Ann. Rev. Nucl. Part. Sci.*, 67, 45
- Moriya T. J., Maeda K., Taddia F., Sollerman J., Blinnikov S. I., Sorokina E. I., 2013, *Mon. Not. Roy. Astron. Soc.*, 435, 1520
- Moriya T. J., Sorokina E. I., Chevalier R. A., 2018, *Space Sci. Rev.*, 214, 59
- Murase K., Thompson T. A., Lacki B. C., Beacom J. F., 2011, *Phys. Rev. D*, 84, 043003
- Necker J., et al., 2022, *Mon. Not. Roy. Astron.*, 516, 2455
- Nicholl M., et al., 2020, *Nature Astronomy*, 4, 893
- Ofek E. O., et al., 2007, *Astrophys. J. Lett.*, 659, L13
- Patnaude D. J., Fesen R. A., 2009, *Astrophys. J.*, 697, 535
- Petropoulou M., Kamble A., Sironi L., 2016, *Mon. Not. Roy. Astron. Soc.*, 460, 44
- Petropoulou M., Coenders S., Vasilopoulos G., Kamble A., Sironi L., 2017, *Mon. Not. Roy. Astron. Soc.*, 470, 1881
- Pititk T., Tamborra I., Angus C. R., Auchettl K., 2022, *Astrophys. J.*, 929, 163
- Predehl P., et al., 2010, in Arnaud M., Murray S. S., Takahashi T., eds., Vol. 7732, *Space Telescopes and Instrumentation 2010: Ultraviolet to Gamma Ray*. SPIE, p. 77320U, doi:10.1117/12.856577, https://doi.org/10.1117/12.856577
- Protheroe R. J., Clay R. W., 2004, *Publ. Astron. Soc. Pac.*, 21, 1
- Rest A., et al., 2011, *Astrophys. J.*, 729, 88
- Reusch S., et al., 2022, *Phys. Rev. Lett.*, 128, 221101
- Rybicki G. B., Lightman A. P., 1986, *Radiative Processes in Astrophysics*
- Sarmah P., Chakraborty S., Tamborra I., Auchettl K., 2022, *J. Cosmology Astropart. Phys.*, 2022, 011
- Sarmah P., Chakraborty S., Tamborra I., Auchettl K., 2023, *arXiv e-prints*, p. arXiv:2303.13576
- Sato T., Katsuda S., Morii M., Bamba A., Hughes J. P., Maeda Y., Ishida M., Frascchetti F., 2018, *Astrophys. J.*, 853, 46
- Schlaflly E. F., Finkbeiner D. P., 2011, *ApJ*, 737, 103
- Schlegel E. M., 1990, *Mon. Not. Roy. Astron. Soc.*, 244, 269
- Schure K. M., Achterberg A., Keppens R., Vink J., 2010, *Mon. Not. Roy. Astron. Soc.*, 406, 2633
- Shappee B. J., et al., 2014, *ApJ*, 788, 48
- Shvartzvald Y., et al., 2023, *arXiv e-prints*, p. arXiv:2304.14482
- Slane P., Lee S. H., Ellison D. C., Patnaude D. J., Hughes J. P., Eriksen K. A., Castro D., Nagataki S., 2015, *Astrophys. J.*, 799, 238
- Smith N., 2017, in Alsabti A. W., Murdin P., eds., *Handbook of Supernovae*. p. 403, doi:10.1007/978-3-319-21846-5_38
- Smith N., Chornock R., Li W., Ganeshalingam M., Silverman J. M., Foley R. J., Filippenko A. V., Barth A. J., 2008, *Astrophys. J.*, 686, 467
- Smith N., Li W., Filippenko A. V., Chornock R., 2011, *Mon. Not. Roy. Astron. Soc.*, 412, 1522
- Stein R., et al., 2023, *Mon. Not. Roy. Astron. Soc.*, 521, 5046
- Sturmer S. J., Skibo J. G., Dermer C. D., Mattox J. R., 1997, *Astrophys. J.*, 490, 619
- Suzuki A., Moriya T. J., Takiwaki T., 2020, *Astrophys. J.*, 899, 56
- Tammi J., Duffy P., 2009, *AIP Conf. Proc.*, 1085, 475
- Villar V. A., Berger E., Metzger B. D., Guillochon J., 2017, *Astrophys. J.*, 849, 70
- Vitagliano E., Tamborra I., Raffelt G., 2020, *Rev. Mod. Phys.*, 92, 45006
- Weaver T. A., 1976, *Astrophys. J.*, 32, 233
- Yuksel H., Kistler M. D., Beacom J. F., Hopkins A. M., 2008, *Astrophys. J. Lett.*, 683, L5
- Zirakashvili V. N., Ptuskin V. S., 2016, *Astropart. Phys.*, 78, 28
- Zyla P., et al., 2020, *PTEP*, 2020, 083C01

A Dependence of the supernova lightcurve properties on the model parameters

In this appendix, we investigate the dependence of the parameters characteristic of the lightcurve on the SN model properties. Figure A1 displays how the rise time t_{rise} (defined in Sec. 3) of the bolometric luminosity depends on the SN parameters of interest. For any fixed combination of E_k , M_{ej} and R_{CSM} , the rise time increases with M_{CSM} , since a denser CSM extends the photon diffusion time. In the left panel, we see that the larger the kinetic energy, the shorter t_{rise} . This is explained by the fact that large shock velocities cause the breakout to happen later and shorten the time that photons take to reach the photosphere. The same trend is expected for decreasing

M_{ej} , as shown in the middle panel, where a mild trend in this direction is noticeable. Furthermore in the BW regime (which corresponds to the breaks in the curves) we see that t_{rise} is independent of M_{ej} (the curves for low M_{ej} saturate at the same value), a trend confirmed by the numerical simulations presented in (Suzuki et al. 2020). In the right panel of Fig. A1, one can observe that for large CSM masses, there is a transition region shifting towards larger R_{CSM} where the trend of t_{rise} is reversed. The reason of this inversion is to be found in the dependence of the photospheric radius on R_{CSM} (see Eq. 12), which for fixed M_{CSM} increases and saturates at a certain R_{CSM} , to turn and decrease for larger CSM radii.

The middle panels of Fig. A1 show that an increase in M_{CSM} makes L_{peak} larger in all cases, since a larger M_{CSM} causes more kinetic energy to be dissipated and radiated. This is true as long as the shock is in the FE regime. In the BW regime, L_{peak} declines with M_{CSM} . The left and middle panels show that the peak luminosity increases with larger ejecta energy and smaller ejecta masses, since both make the shock velocity larger and thus more energetic. In the BW regime, the peak luminosity becomes independent of the ejecta mass, as confirmed by the saturation to the same branch for low M_{ej} . The right panel shows that the brightest lightcurves are obtained when the CSM is more compact, i.e. for the smallest R_{CSM} (apart from the transition region visible for large M_{CSM} , due to the transition into the BW regime).

The bottom panels show the trend of $E_{\text{diss,thick}}$. The dissipated energy in the optically thick part of the CSM increases with M_{CSM} , is very large for small M_{ej} and R_{CSM} , since the first allows for high shock velocity, and the second for very compact region, and thus high densities.

B Dependence of the maximum proton energy on the supernova model parameters

In this appendix, we analyze the dependence of the maximum $E_{\text{p,max}}$ on the SN model parameters. To do so, we first highlight the dependence on the SN parameters of the main timescales entering the problem. From Eqs. 10 and 11, we see that the plasma cooling timescale scales as:

$$t_{\text{cool}} \propto \frac{1}{n_{\text{sh}}} \times \begin{cases} v_{\text{sh}}^{16/5} & \text{if } 10^5 < T \lesssim 4.7 \times 10^7 \text{ K} \\ v_{\text{sh}} & \text{if } T > 4.7 \times 10^7 \text{ K} . \end{cases} \quad (\text{B1})$$

For the wind scenario, it becomes

- for $R < R_{\text{dec}}$:

$$t_{\text{cool}} \propto \left(\frac{R_{\text{CSM,w}}}{M_{\text{CSM,w}}} \right) \times \begin{cases} R^{54/35} & \text{if } 10^5 < T \lesssim 4.7 \times 10^7 \text{ K} \\ R^{13/7} & \text{if } T > 4.7 \times 10^7 \text{ K} . \end{cases} \quad (\text{B2})$$

- for $R > R_{\text{dec}}$:

$$t_{\text{cool}} \propto \left(\frac{R_{\text{CSM,w}}}{M_{\text{CSM,w}}} \right) \times \begin{cases} R^{2/5} & \text{if } 10^5 < T \lesssim 4.7 \times 10^7 \text{ K} \\ R^{3/2} & \text{if } T > 4.7 \times 10^7 \text{ K} . \end{cases} \quad (\text{B3})$$

For the shell scenario, it is

- for $R < R_{\text{dec}}$:

$$t_{\text{cool}} \propto \left(\frac{R_{\text{CSM,s}}^3}{M_{\text{CSM,s}}} \right) \times \begin{cases} R^{-48/35} & \text{if } 10^5 < T \lesssim 4.7 \times 10^7 \text{ K} \\ R^{-3/7} & \text{if } T > 4.7 \times 10^7 \text{ K} . \end{cases} \quad (\text{B4})$$

- for $R > R_{\text{dec}}$:

$$t_{\text{cool}} \propto \left(\frac{R_{\text{CSM,s}}^3}{M_{\text{CSM,s}}} \right) \times \begin{cases} R^{-24/5} & \text{if } 10^5 < T \lesssim 4.7 \times 10^7 \text{ K} \\ R^{-3/2} & \text{if } T > 4.7 \times 10^7 \text{ K} . \end{cases} \quad (\text{B5})$$

The acceleration time scales as $t_{\text{acc}} \propto E_{\text{p}} v_{\text{sh}}^{-3} n_{\text{sh}}^{-1/2}$, given $B \propto v_{\text{sh}} n_{\text{sh}}^{1/2}$. For the wind scenario it is

$$t_{\text{acc}} \propto \left(\frac{R_{\text{CSM,w}}}{M_{\text{CSM,w}}} \right)^{1/2} E_{\text{p}} \times \begin{cases} R^{10/7} & \text{if } R < R_{\text{dec}} \\ R^{5/2} & \text{if } R > R_{\text{dec}} ; \end{cases} \quad (\text{B6})$$

while for the shell scenario, it is

$$t_{\text{acc}} \propto \left(\frac{R_{\text{CSM,s}}^3}{M_{\text{CSM,s}}} \right)^{1/2} E_{\text{p}} \times \begin{cases} R^{9/7} & \text{if } R < R_{\text{dec}} \\ R^{9/2} & \text{if } R > R_{\text{dec}} . \end{cases} \quad (\text{B7})$$

The proton-proton interaction time $t_{\text{pp}} = (cn_{\text{sh}}\sigma_{\text{pp}})^{-1}$ is

$$t_{\text{pp}} \propto \begin{cases} \frac{R_{\text{CSM,w}}}{M_{\text{CSM,w}}} \times R^2 & \text{for the wind} \\ \frac{R_{\text{CSM,s}}^3}{M_{\text{CSM,s}}} & \text{for the shell} . \end{cases} \quad (\text{B8})$$

Using the relations above, we can investigate how $E_{\text{p,max}}$ depends on the SN model parameters and how it evolves with the shock radius. If t_{cool} is the $\min[t_{\text{cool}}, t_{\text{dyn}}, t_{\text{pp}}]$, the maximum proton energy is determined by $t_{\text{acc}} = t_{\text{cool}}$. For the wind scenario,

- for $R < R_{\text{dec}}$:

$$E_{\text{p,max}} \propto \left(\frac{R_{\text{CSM,w}}}{M_{\text{CSM,w}}} \right)^{1/2} \times \begin{cases} R^{4/35} & \text{if } 10^5 < T \lesssim 4.7 \times 10^7 \text{ K} \\ R^{3/7} & \text{if } T > 4.7 \times 10^7 \text{ K} ; \end{cases} \quad (\text{B9})$$

- for $R > R_{\text{dec}}$:

$$E_{\text{p,max}} \propto \left(\frac{R_{\text{CSM,w}}}{M_{\text{CSM,w}}} \right)^{1/2} \times \begin{cases} R^{-21/10} & \text{if } 10^5 < T \lesssim 4.7 \times 10^7 \text{ K} \\ R^{-1} & \text{if } T > 4.7 \times 10^7 \text{ K} . \end{cases} \quad (\text{B10})$$

For the shell scenario, instead, it is

- for $R < R_{\text{dec}}$:

$$E_{\text{p,max}} \propto \left(\frac{R_{\text{CSM,s}}^3}{M_{\text{CSM}}} \right)^{1/2} \times \begin{cases} R^{-93/35} & \text{if } 10^5 < T \lesssim 4.7 \times 10^7 \text{ K} \\ R^{-12/7} & \text{if } T > 4.7 \times 10^7 \text{ K} ; \end{cases} \quad (\text{B11})$$

- for $R > R_{\text{dec}}$:

$$E_{\text{p,max}} \propto \left(\frac{R_{\text{CSM,s}}^3}{M_{\text{CSM}}} \right)^{1/2} \times \begin{cases} R^{-93/10} & \text{if } 10^5 < T \lesssim 4.7 \times 10^7 \text{ K} \\ R^{-6} & \text{if } T > 4.7 \times 10^7 \text{ K} . \end{cases} \quad (\text{B12})$$

If t_{pp} corresponds to the $\min[t_{\text{cool}}, t_{\text{dyn}}, t_{\text{pp}}]$, then the maximum proton energy is determined by $t_{\text{acc}} = t_{\text{pp}}$ and can be written for the wind scenario as

$$E_{\text{p,max}} \propto \left(\frac{R_{\text{CSM,w}}}{M_{\text{CSM,w}}} \right)^{1/2} \times \begin{cases} R^{4/7} & \text{for } R < R_{\text{dec}} \\ R^{-1/2} & \text{for } R > R_{\text{dec}} , \end{cases} \quad (\text{B13})$$

and for the shell scenario as

$$E_{\text{p,max}} \propto \left(\frac{R_{\text{CSM,s}}^3}{M_{\text{CSM,s}}} \right)^{1/2} \times \begin{cases} R^{-9/7} & \text{for } R < R_{\text{dec}} \\ R^{-9/2} & \text{for } R > R_{\text{dec}} . \end{cases} \quad (\text{B14})$$

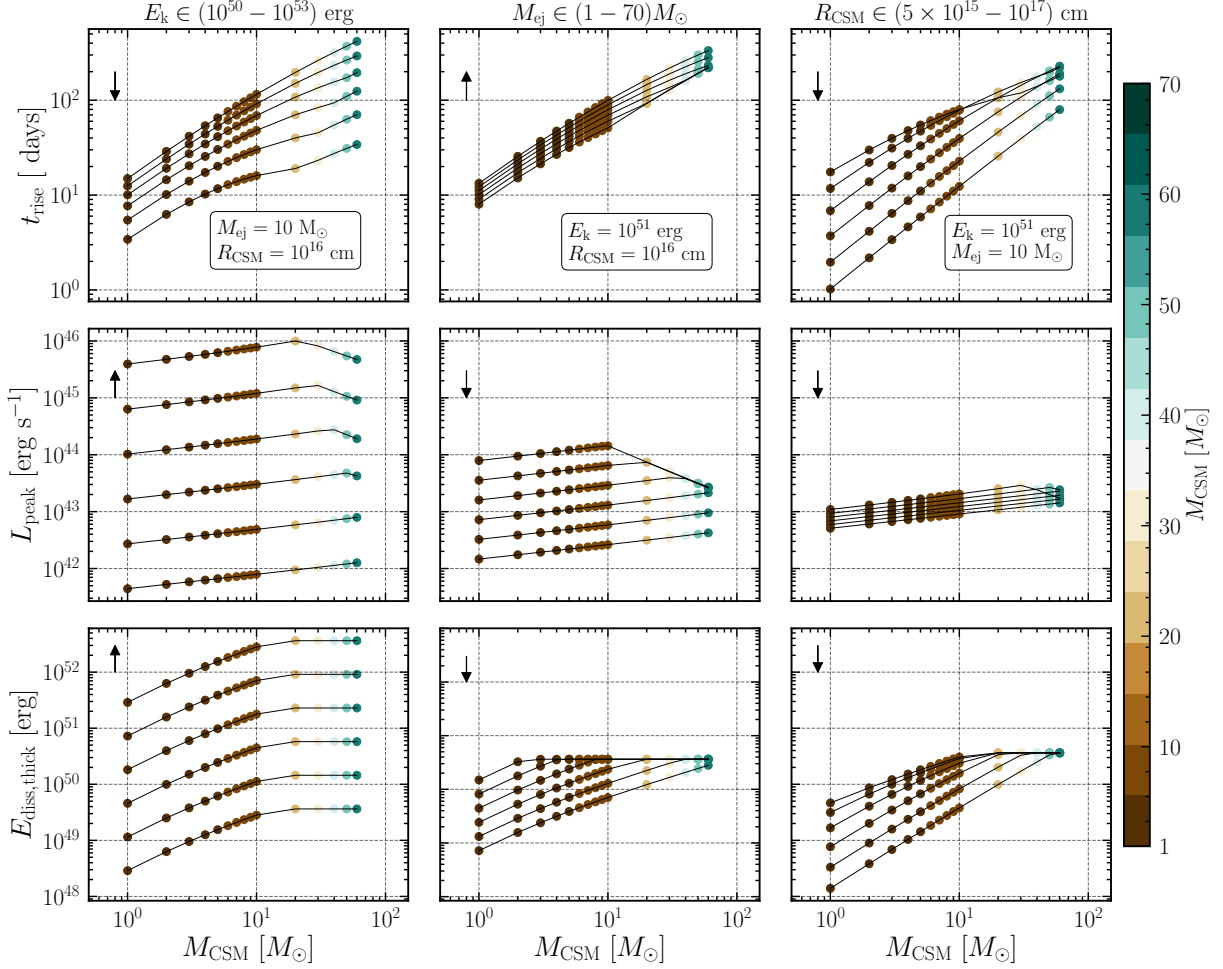


Figure A1. Rise time of the bolometric lightcurve (top panels), bolometric peak luminosity (middle panels), dissipated energy in the optically thick part of the CSM envelope (bottom panels) as functions of the CSM mass and E_k (left panels, for fixed M_{ej} and R_{CSM}), the ejecta mass (middle panels, for fixed E_k and R_{CSM}), and R_{CSM} (right panels, for fixed E_k and M_{ej}), respectively. In each panel, the arrow indicates the direction of increase of the parameter under investigation, e.g. in the left panel of the first row, t_{rise} decreases for increasing E_k , for fixed M_{CSM} ; t_{rise} increases with M_{CSM} since a denser CSM envelope increases the optical depth and delays the photon escape. From the top left and middle panels, we see that for increasing E_k or decreasing M_{ej} , the diffusion time becomes shorter. Indeed both the increase of E_k and the decrease of M_{ej} are responsible for an increase of the shock velocity, which in turn causes the radius where the photon diffusion velocity exceeds the shock velocity to shift outwards. In the top right panel, we observe that for small R_{CSM} an initial increase of t_{rise} , which declines again for larger CSM radii. This transition region is related to the photosphere dependence on M_{CSM} and R_{CSM} . For what concerns L_{peak} , in all three middle panels we see that L_{peak} initially increases with M_{CSM} in the FE regime. When transitioning to the BW regime (indicated by the breaks in the curves), a saturation of the radiated energy occurs and this, together with the increase of t_{rise} , causes L_{peak} to drop as M_{CSM} increases. Larger E_k and smaller M_{ej} are responsible for a larger shock velocity, and thus an increase of L_{peak} , as it can be seen in the left and middle panels. In the right middle panel, we observe that small R_{CSM} , for fixed M_{CSM} , make the medium denser and therefore it is easier to dissipate the ejecta energy, leading to an increase of L_{peak} . Similarly, $E_{diss,thick}$ increases with M_{CSM} , and saturates to a constant fraction of E_k in the BW regime. The dots are colored according to the M_{CSM} value, as shown in the color bar.

Finally, if t_{dyn} corresponds to $\min[t_{cool}, t_{dyn}, t_{pp}]$, the maximum proton energy is determined by $t_{acc} = t_{dyn}$ and for the wind scenario it is

$$E_{p,max} \propto \left(\frac{M_{CSM,w}}{R_{CSM,w}} \right)^{1/2} \times \begin{cases} R^{-2/7} & \text{for } R < R_{dec} \\ R^{-1} & \text{for } R > R_{dec} \end{cases} \quad (B15)$$

while, for the shell scenario, it is

$$E_{p,max} \propto \left(\frac{M_{CSM,s}}{R_{CSM,s}^3} \right)^{1/2} \times \begin{cases} R^{1/7} & \text{for } R < R_{dec} \\ R^{-2} & \text{for } R > R_{dec} \end{cases} \quad (B16)$$

Note that we assume constant $\sigma_{pp} \sim 3 \times 10^{-26} \text{ cm}^2$ for the sake of simplicity in this appendix in order to obtain the above analytical relations.

We immediately see from the relations above that for the wind scenario, independently on the cooling mechanism, the maximum proton energy has a decreasing trend with R in the deceleration phase ($R > R_{dec}$). However, in the ejecta-dominated phase ($R < R_{dec}$), the maximum proton energy always increases, except for the case in which the adiabatic cooling is dominant (Eq. B15). Finally, in the shell scenario, $E_{p,max}$ always decreases, apart from the case where t_{cool} and t_{pp} are too long compared to the dynamical time, and it slowly increases in the free-expansion phase.

We define R_{cool} as the radius where $t_{dyn} = t_{cool}$, and R_{pp} the radius where $t_{dyn} = t_{pp}$. The maximum value of $E_{p,max}$, denoted as $E_{p,max}^*$, can be achieved at any of the following radii: R_{bo} , R_{cool} , R_{pp} , R_{dec} , or R_{CSM} . There are various configurations of such radii. If for

example $R_{\text{bo}} < R_{\text{cool}} < R_{\text{pp}} < R_{\text{CSM}} < R_{\text{dec}}$, and both $t_{\text{dyn}} < t_{\text{cool}}$ for $R > R_{\text{cool}}$ and $t_{\text{dyn}} < t_{\text{pp}}$ for $R > R_{\text{pp}}$, then the maximum $E_{\text{p,max}}$ is obtained at R_{pp} .

Note that this procedure serves to inspect the dependence of the maximum proton energy analytically. However, the total cooling time is the sum of t_{dyn} and t_{pp} or t_{cool} and t_{pp} ; since the energy dependence of t_{pp} increases slightly at higher energies, the value of $E_{\text{p,max}}^*$ that we find is underestimated by a few percent in the transition region $t_{\text{dyn}} \sim t_{\text{cool}}$ and at very large energies. Figure B1 displays how $E_{\text{p,max}}^*$ depends on the SN parameters. The most promising configurations that allow to reach large $E_{\text{p,max}}^*$ are the ones with large E_{k} and low M_{CSM} (left panel), or low M_{ej} and low M_{CSM} (middle panel), or high R_{CSM} and low M_{CSM} (right panel), which maximize the acceleration rate and minimize the energy loss rate.

For the fiducial parameters adopted in each panel of Fig. B1, total energies $\gtrsim 10^{51}$ erg, relatively low ejecta ($\lesssim 20 M_{\odot}$), CSM masses ($\lesssim 10 M_{\odot}$), and extended CSM envelopes ($\gtrsim 10^{16}$ cm) are required to obtain protons with \sim PeV energy. Furthermore, as shown through the gray contour lines, which display $t|_{E_{\text{p,max}}^*} - t_{\text{peak}}$ (where $t|_{E_{\text{p,max}}^*}$ is the time at which the maximum proton energy is reached), the maximum $E_{\text{p,max}}^*$ is achieved at relatively late times [$O(100 \text{ days})$] with respect to the peak time $t_{\text{peak}} = t_{\text{bo}} + t_{\text{rise}}$. Such longer timescales are expected for low kinetic energies of the ejecta, and large M_{ej} and R_{CSM} . Only the configurations with large CSM mass, due to the onset of the decelerating phase, are expected to invert the increasing trend of $E_{\text{p,max}}^*$ before the lightcurve reaches its peak.

C Constant density scenario

In this appendix, we explore the dependence of neutrino production in the scenario of a radially independent CSM mass distribution. We follow a similar approach to the wind-profile case discussed in Sec. 5.2. Specifically, we investigate the connection between the total energy in neutrinos ($\mathcal{E}_{\nu+\bar{\nu}}$, see Eq. 22) with $E_{\nu} \geq 1 \text{ TeV}$. The results are shown in Fig. C1.

We exclude from our investigation the region of the SN parameter space where the maximum achievable proton energy is $E_{\text{p,max}}^* \leq 10 \text{ TeV}$. Additionally, we disregard parameters that lead to a shock breakout at the surface of the progenitor star ($R_{\text{bo}} \equiv R_{\star}$), as indicated by the beige region in the contour plots. In this work, our focus is on the parameter space that results in the shock breakout occurring inside the CSM envelope. This is the first difference with the wind case, where the much higher density at smaller radii cause the shock to occur inside the wind for all the considered parameters. Isocontours of $E_{\text{p,max}}^*$ (first row), the rise time t_{rise} (second row), and the bolometric peak L_{peak} (third row) are also displayed on top of the $\mathcal{E}_{\nu+\bar{\nu}}$ colormap in Fig. C1.

The dependence of $\mathcal{E}_{\nu+\bar{\nu}}$ on the SN model parameters is analogous to the wind scenario. Indeed we see that in all panels of Fig. C1, $\mathcal{E}_{\nu+\bar{\nu}}$ increases with M_{CSM} , namely with larger target proton numbers, and then saturates once the critical ρ_{CSM} is reached. Beyond such critical density, pp interactions or the cooling of thermal plasma becomes too strong, limiting the maximum achievable proton energy, and thus the neutrino outcome. From the contour lines in each panel, analogously to the wind case, we see that the optimal configuration for what concerns neutrino production, results from large E_{k} , $M_{\text{CSM}} \gtrsim M_{\text{ej}}$, and R_{CSM} larger as M_{CSM} increases.

We see from Fig. C1 that we do not have the same regions of the parameter space excluded as in the wind case (see Fig. 5) that lead to $E_{\text{p,max}}^* \leq 10 \text{ TeV}$. Indeed in a constant density shell the proton maximum energy has a rather different dependence especially on the

radius as discussed in Appendix B. This leads to overall higher values of $E_{\text{p,max}}^*$ in the parameter space, as well as the times at which they are achieved during the shock evolution. Most of the parameter space in all panels leads to $\Delta t_{\text{pk}} = t|_{E_{\text{p,max}}^*} - t_{\text{peak}} < 0$ (see Fig. B1 for the wind case). This means that in the constant density scenario most of the energetic neutrinos are produced earlier than the bolometric peak.

With respect to the wind scenario, another difference lies in the relation between t_{rise} and L_{peak} , as can be seen from the second and third row of Fig. C1. In the case of a constant density shell, the CSM density is considerably lower. Consequently, the shock breakout tends to occur earlier than in the wind scenario, resulting in significantly smaller peak luminosities across a significant portion of the parameter space. Nonetheless, the lower CSM density leads to larger deceleration radii compared to the wind case. As a result, a larger M_{CSM} is required to enter the decelerating regime, delaying the transition to the decreasing trend of L_{peak} with M_{CSM} in the blast-wave regime (as observed in the wind case in Fig. A1). As for t_{rise} , lower CSM densities result in longer photon mean free paths, enabling faster diffusion through the CSM envelope. Furthermore, as shown in the second row of Fig. C1, t_{rise} increases with M_{CSM} , but remains independent on M_{ej} and E_{k} for most of the parameter space. This is explained because R_{bo} is significantly smaller than R_{ph} , making the diffusion time unaffected by the shock velocity.

In summary, similar to the wind scenario, large $\mathcal{E}_{\nu+\bar{\nu}}$ is expected for large SN kinetic energy ($E_{\text{k}} \gtrsim 10^{51} \text{ erg}$), small ejecta mass ($M_{\text{ej}} \lesssim 10 M_{\odot}$), and large CSM radii, $R_{\text{CSM}} \gtrsim 10^{16} \text{ cm}$. Unlike in the wind case, a larger range of M_{CSM} leads to comparable predictions, even if scenarios with $M_{\text{CSM}} \gg M_{\text{ej}}$ would limit neutrino production. Such parameters imply large bolometric luminosity peak ($L_{\text{peak}} \gtrsim 10^{43} - 10^{44} \text{ erg}$) and relatively long rise times ($t_{\text{rise}} \gtrsim 10 - 90 \text{ days}$). In the shell case, large t_{rise} do not necessarily correspond to low $\mathcal{E}_{\nu+\bar{\nu}}$, as it is the case for the wind scenario. Furthermore, energetic neutrinos are produced at early times. Hence, if neutrinos should be observed from long-rising optical lightcurves relatively soon with respect to the optical peak, this might hint towards a constant density of the CSM envelope.

This paper has been typeset from a \LaTeX file prepared by the author.

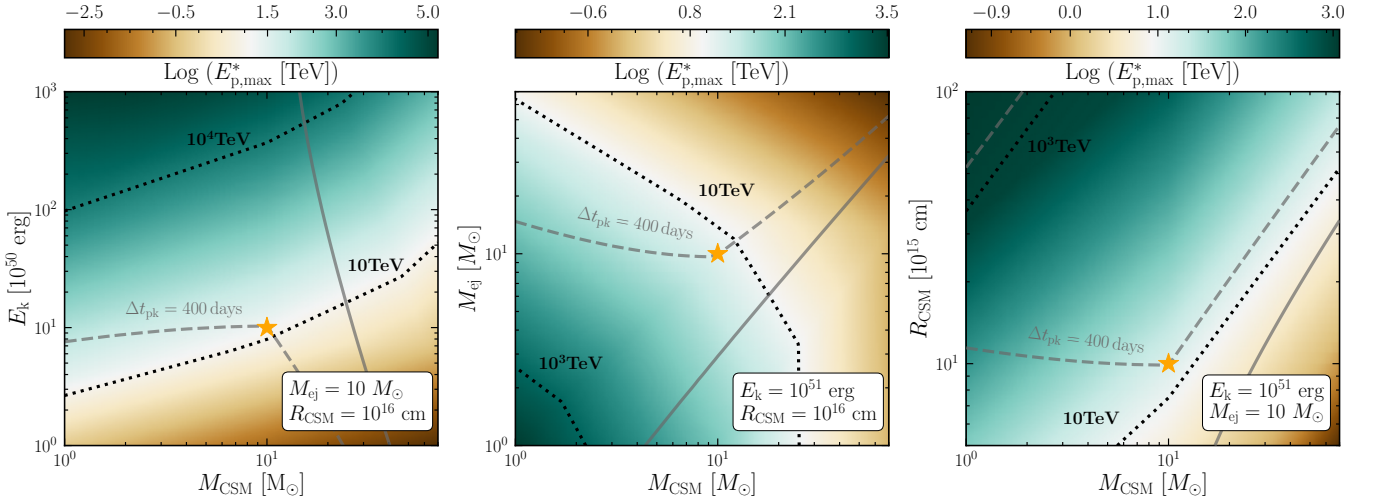


Figure B1. Contour plots of the maximum proton energy $E_{p,\max}^*$ reached throughout the evolution of the shock in the wind scenario, in the plane spanned by M_{CSM} and E_k (left panel), M_{ej} (middle panel), and R_{CSM} (right panel). The dotted contours mark isocontours of $E_{p,\max}^*$ to guide the eye. The largest proton energies can be achieved with large E_k and small M_{ej} , both maximizing v_{sh} , and thus the acceleration rate; low M_{CSM} and/or large R_{CSM} , both making the CSM less dense, and thus the proton energy losses less severe. For each panel, the gray line represents $\Delta t_{\text{pk}} = t|_{E_{p,\max}^*} - t_{\text{peak}}$, i.e. the time at which the maximum proton energy is reached with respect to the bolometric peak of the lightcurve. The solid gray lines correspond to $\Delta t_{\text{pk}} = 0$. From the dashed gray line, we can see that the largest time interval is expected for low E_k , and large M_{ej} and R_{CSM} . The parameter space between the solid and the dashed gray lines leads to $0 < \Delta t_{\text{pk}} < 400$ days, which is the follow-up time window adopted for SNe. The orange star marks our benchmark scenario (see Table 1).

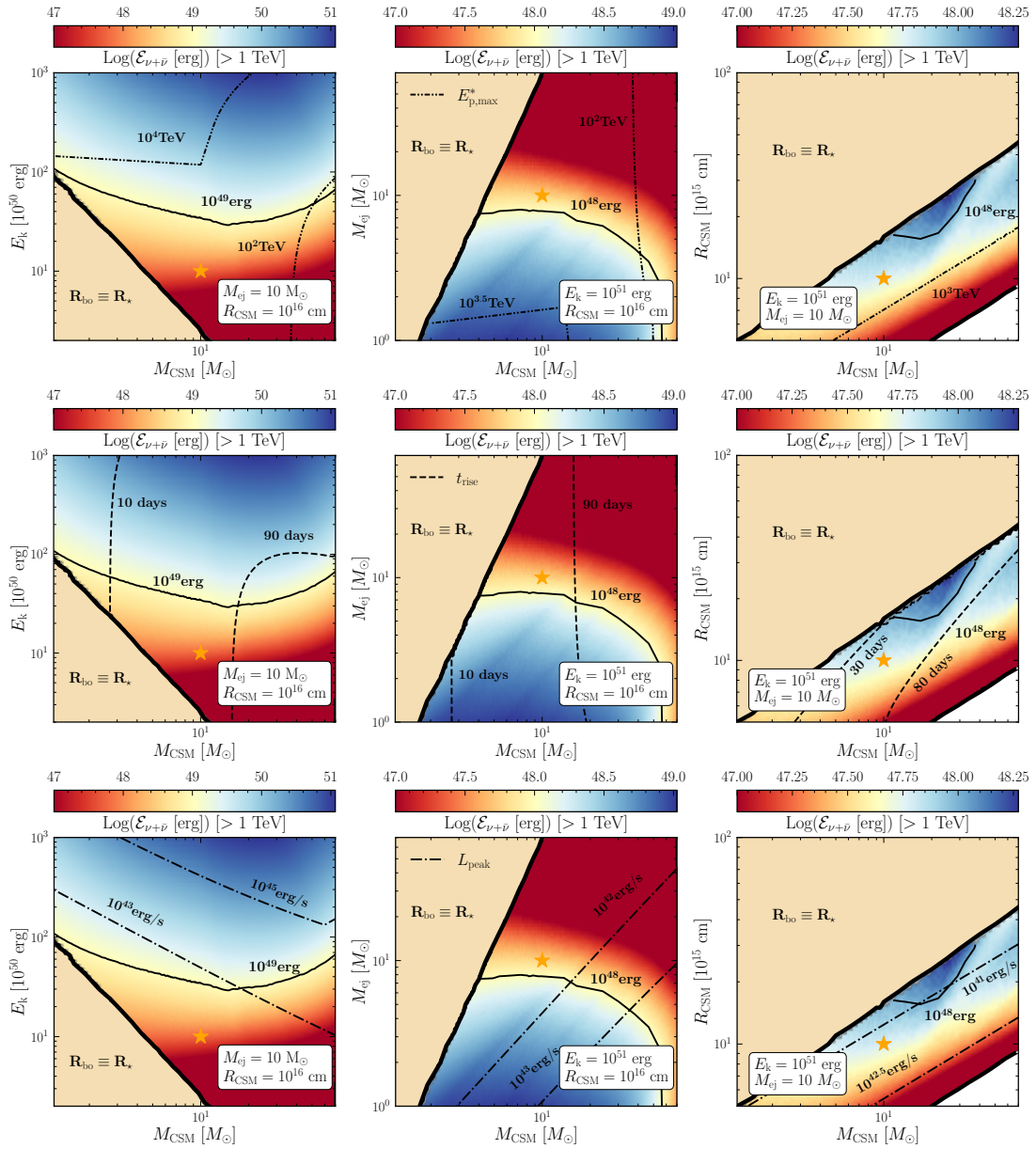


Figure C1. The same as in Fig. 5, but for the constant density shell scenario. The beige region has been excluded from our investigation since here the breakout of the shock does not occur in the CSM shell, but at the radius of the progenitor star. The white region, visible only in the lower right corner of the third column, has instead been excluded because leading to $E_{p,\max}^* < 10\text{TeV}$. The SN configurations leading to the largest outcomes in neutrinos are similar to the ones in the wind case, and are given by large SN kinetic energies ($E_k \gtrsim 10^{51}\text{ erg}$), small ejecta masses ($M_{ej} \lesssim 10 M_\odot$), intermediate CSM masses with respect to M_{ej} ($1 M_\odot \lesssim M_{CSM} \lesssim 30 M_\odot$), and relatively large CSM extent ($R_{CSM} \gtrsim 10^{16}\text{ cm}$).